

## **Chapter V**

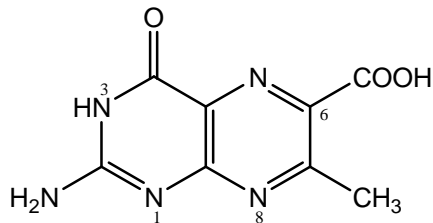
**Conformational control of pterin- and nickel- centred  
redox reactions of mixed ligand nickel-pterin  
complexes: synthesis, structural, chiroptical and  
reactivity studies.**

## Abstract

Two new nickel(II) complexes having the identical chemical composition  $[\text{Ni}(\text{L})(\text{pn})(\text{H}_2\text{O})] \cdot 5\text{H}_2\text{O}$  have been synthesized and characterized, where  $\text{L}^{2-}$  is the anion of 7-methylpterin-6-carboxylic acid and 'pn' represents R-(+)-pn or S-(-)-pn. Circular dichroism spectroscopy establish their chiral nature which can be traced to the conformation of their 'pn' chelate rings. Reactivities of these two complex have been studied using both group and group/electron transfer reagents. For group and group/electron transfer reagents (imidazole,  $\text{NaBH}_4$ , bromobenzene/ $\text{O}_2$ ) the  $k_{\text{obs}}$  values are of the order of  $10^{-3}\text{s}^{-1}$ ; for an electron transfer agent like  $\text{K}_3[\text{Fe}(\text{CN})_6]$ , the  $k_{\text{obs}}$  value has an order of  $10^{-2}\text{s}^{-1}$ . In all these cases the  $\Delta S^\ddagger$  value is negative, indicating the associative nature of such reactions. The reaction profiles of these two chiral complexes towards each of the above reagents are different highlighting the conformational control of the 'pn' chelate ring in such cases. The small band gaps between some of their frontier orbitals are partly responsible for such unique redox activities.

## Introduction

In pursuance of our continued interest in redox chemistry of nickel [Ni(I) and Ni(II) states] with the redox non-innocent pterin ligand 7-methylpterin-6-carboxylic acid ( $\text{H}_2\text{L}$ , **1**), we present here our studies on two new nickel(II) complexes, with the chiral ancillary ligands R-(+)-1, 2 – diaminopropane and S-(-)-1, 2 – diaminopropane.



The pterin ligand (**1**, H<sub>2</sub>L)

The ancillary ligands have been chosen purposefully for exploring the chelate ring conformational control of redox activity of the resulting complexes. Once again, the methods and reagents have been chosen carefully for this purpose.

Finally, the molecular properties have been analyzed on the basis of electronic structures obtained by DFT method.

## Experimental

**Materials:** Reagent grade chemicals were used as received. Solvents were purified before use following literature procedures<sup>20</sup>. Kinetic and electro-chemical studies were performed in spectroscopy grade methanol and DMSO respectively (SRL, Mumbai); Bu<sub>4</sub>NClO<sub>4</sub> (TBAP) were obtained from published methods<sup>72</sup>. R-(+)- 1, 2- diaminopropane [R-(+)-pn] and S-(-) – 1, 2 – diaminopropane [S-(-)-pn] were obtained from Sigma Aldrich. NiSO<sub>4</sub>, 7H<sub>2</sub>O, K<sub>3</sub>Fe(CN)<sub>6</sub>, imidazole (Im) and NaBH<sub>4</sub> were obtained from SRL, Mumbai. H<sub>2</sub>L was prepared by published procedure.<sup>19</sup>

**Method:** The two new complexes characterized x-ray crystallographically and also by different physico-chemical methods including elemental analysis, ESIMS, IR, UV-Vis and <sup>1</sup>H NMR data. Details about the instrumental measurements have been presented in earlier chapters, especially chapter III.

## Synthesis of the complexes

### **2-amino-4-hydroxy-7-methylpteridine-6-carboxylic acid sesquihydrate (C<sub>8</sub>H<sub>7</sub>N<sub>5</sub>O<sub>3</sub> · 1.5H<sub>2</sub>O)**

**(1)**

The above pterin ligand (H<sub>2</sub>L · 1.5 H<sub>2</sub>O) was obtained by published procedure.<sup>19</sup>

### **[Ni(C<sub>8</sub>H<sub>5</sub>N<sub>5</sub>O<sub>3</sub>)(R- (+) -C<sub>3</sub>H<sub>10</sub>N<sub>2</sub>)(H<sub>2</sub>O)]. 5H<sub>2</sub>O (2)**

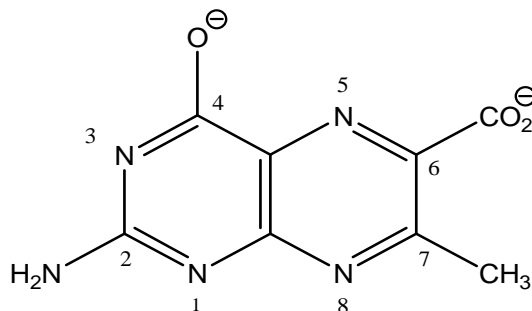
The complex was prepared by the slow addition of an aqueous alkaline solution (NaOH: 44mg, 1.1 mmol) of the pterin ligand (124mg, 0.5mmol) to a well-stirred warm (323K; paraffin oil bath) aqueous reaction mixture containing NiSO<sub>4</sub> · 7H<sub>2</sub>O (140mg, 0.5mmol) and R- (+)-pn (39mg, 0.6mmol) under subdued light; final volume was 35 ml. The pH was adjusted to 9.2 and the stirring was continued for 3h. Upon standing, the reaction medium deposited golden-yellow crystals after 2 days, which were suitable for single crystal x-ray diffraction yield, 30%.

Analytically pure compound could be obtained by filtration, repeated washing with small quantities of water and drying in vacuo over silica gel. Analysis, calculated for C<sub>11</sub>H<sub>28</sub>N<sub>7</sub>O<sub>9</sub>Ni: C 28.65, H 6.07, N 21.27 %; found: C 28.91, H 5.74, N 20.94 %. UV – VIS absorption bands [CH<sub>3</sub>OH, λ<sub>max</sub><sup>nm</sup>(logε)]: 211(4.51), 243sh(4.15), 272(4.13), 277(4.54), 349(4.31), 365(3.89), 764(1.24), 895(1.93)

### **[Ni(C<sub>8</sub>H<sub>5</sub>N<sub>5</sub>O<sub>3</sub>)(S-(-)- C<sub>3</sub>H<sub>10</sub>N<sub>2</sub>)(H<sub>2</sub>O)]. 5H<sub>2</sub>O (3)**

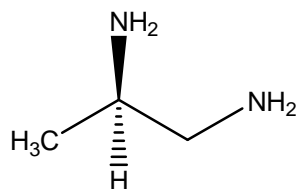
The complex was prepared by the slow addition of an aqueous alkaline solution (NaOH: 44mg, 1.1 mmol) of the pterin ligand (124mg, 0.5mmol) to a well-stirred warm (323K; paraffin oil bath) aqueous reaction mixture containing NiSO<sub>4</sub> · 7H<sub>2</sub>O (140mg, 0.5mmol) and S -(-)-pn (39mg, 0.6mmol) under subdued light; final volume was 35 ml. The pH was adjusted to 9.2 and the stirring was continued for 3h. Upon standing, the reaction medium deposited golden-yellow crystals after 2 days, which were suitable for single crystal x-ray diffraction yield, 30%.

Analytically pure compound could be obtained by filtration, repeated washing with small quantities of water and drying in vacuo over silica gel. Analysis, calculated for  $C_{11}H_{28}N_7O_9Ni$ : C 28.65, H 6.07, N 21.27 %; found: C 29.34, H 5.82, N 21.16 %. UV – VIS absorption bands [ $CH_3OH$ ,  $\lambda_{max}^{nm}(\log\epsilon)$ ]: 273(4.36), 365(3.98), 512sh(1.02), 640sh(1.06), 707(1.22), 728(1.44), 802(1.53), 911sh(0.78), 1053sh(1.35)



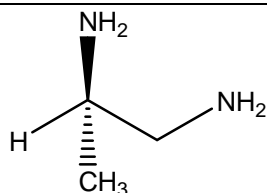
The pterin ligand ( $H_2L$ ) anion ( $L^{2-}$ ,  $C_8H_5N_5O_3$ )

**Scheme V- 1**



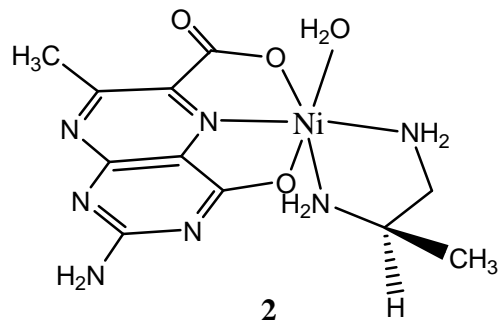
R-(+)- 1, 2- diaminopropane[R-(+)-pn]

**Scheme V-2**

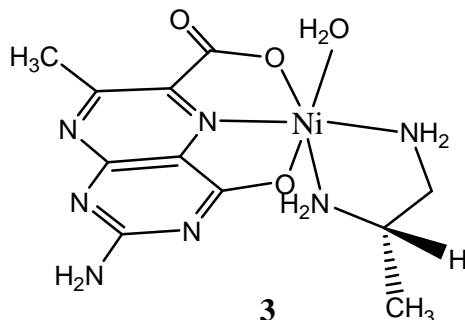


S-(-)- 1, 2- diaminopropane[S-(-)-pn]

**Scheme V-3**



**Scheme V-4**



**Scheme V-5**

## Results and Discussion

These two new Ni(II) mixed ligand complexes (Scheme V-4 and Scheme V-5) could be crystallized out of the aqueous alkaline medium. Careful control of the reaction conditions led to their isolation in the chiral form, using the chiral ancillary ligands R-(+)-pn and S-(-)-pn respectively [Scheme V-2 and Scheme V-3]. Analytically pure samples could be obtained through washing the crystals with water and drying in vacuo; such that samples are suitable for microanalytical purpose as well as electrospray ionisation mass spectral data (ESIMS) collection.

These chiral compounds afford valuable chiroptical, electrochemical and redox reactivity data, as discussed below.

### **Molecular structure of [Ni(C<sub>8</sub>H<sub>5</sub>N<sub>5</sub>O<sub>3</sub>)(R-(+)-C<sub>3</sub>H<sub>10</sub>N<sub>2</sub>)(H<sub>2</sub>O)]. 5H<sub>2</sub>O (2) and [Ni(C<sub>8</sub>H<sub>5</sub>N<sub>5</sub>O<sub>3</sub>)(S-(-)-C<sub>3</sub>H<sub>10</sub>N<sub>2</sub>)(H<sub>2</sub>O)]. 5H<sub>2</sub>O (3)**

Figure V-1 and V-2 represent the molecular structures of the two new Ni(II) complexes. Table V-1 shows their crystallographic data and structure refinements. Their geometry parameters, hydrogen atom coordinates are presented in Table V-2, V-3, V-4 and V-5

respectively. The crystal packing diagrams and unit cells of **2** and **3** are represented in Figure V-3, V – 4, V – 5 and V – 6, respectively.

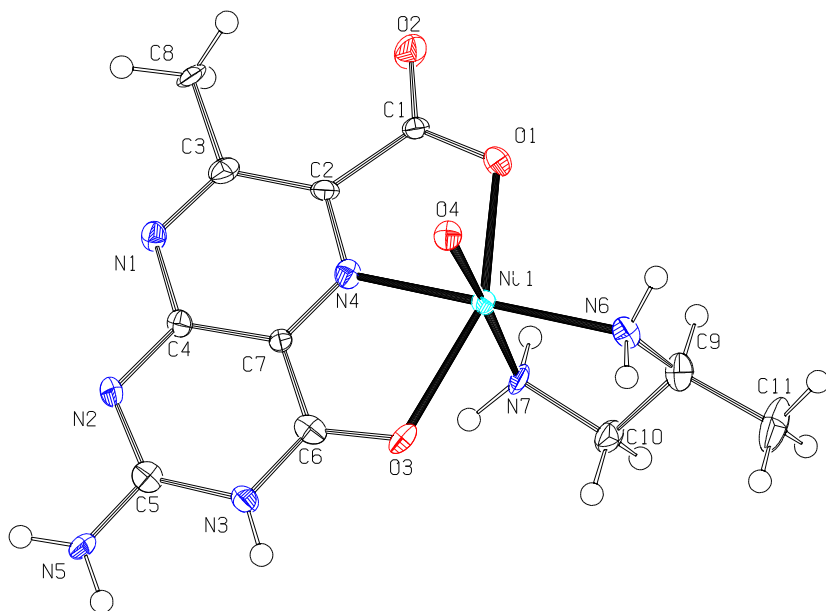


**Figure V-1.** ORTEP diagram of **2** probability at 50% thermal ellipsoide; lattice water molecules are omitted for clarity.

---

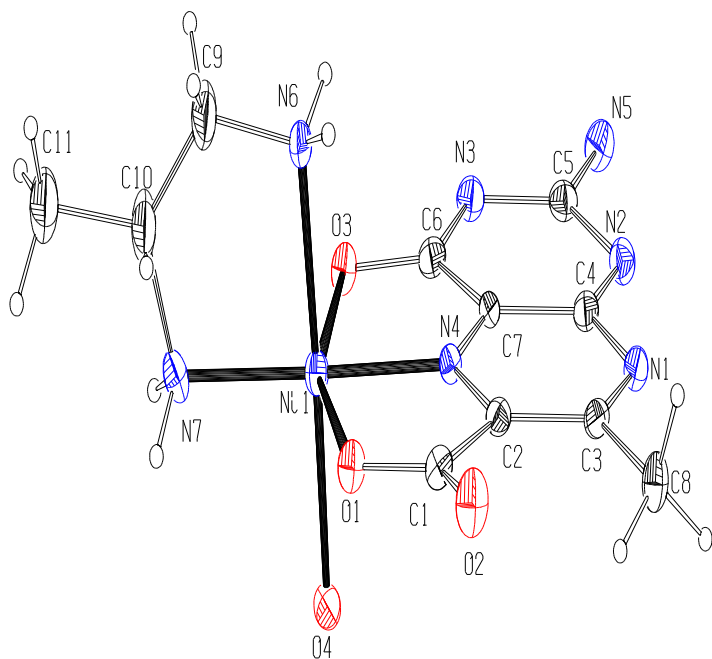


**Figure V- 2.** ORTEP diagram of **3** probability at 50% thermal ellipsoide; lattice water molecules are omitted for clarity.

---

**Table V-1. Crystal data and structure refinement for 2 and 3**

<b>Identification code</b>	<b>2</b>	<b>3</b>
<b>Empirical formula</b>	C <sub>22</sub> H <sub>32</sub> N <sub>14</sub> Ni <sub>2</sub> O <sub>18</sub>	C <sub>11</sub> H <sub>13</sub> N <sub>7</sub> NiO <sub>9</sub>
<b>Formula weight</b>	898.04	445.99
<b>Temperature/K</b>	110(2)	293(2)
<b>Crystal system</b>	Monoclinic	Monoclinic
<b>Space group</b>	P2 <sub>1</sub>	P2 <sub>1</sub> /c
<b>a/Å</b>	10.4777(14)	14.47(2)
<b>b/Å</b>	13.3994(17)	13.59(2)
<b>c/Å</b>	14.2435(18)	10.632(17)
<b>α/°</b>	90.00	90.00
<b>β/°</b>	102.434(2)	102.04(2)
<b>γ/°</b>	90.00	90.00
<b>Volume/Å<sup>3</sup></b>	1952.8(4)	2045(5)
<b>Z</b>	2	4
<b>ρ<sub>calc</sub>/cm<sup>3</sup></b>	1.527	1.449
<b>μ/mm<sup>-1</sup></b>	1.052	1.004
<b>F(000)</b>	924.0	912.0
<b>Crystal size/mm<sup>3</sup></b>	0.33 × 0.20 × 0.06	0.21 × 0.12 × 0.03
<b>Radiation</b>	MoKα (λ = 0.71073)	MoKα (λ = 0.71073)
<b>2θ range for data collection/°</b>	2.92 to 56.52	4.16 to 49.98

<b>Index ranges</b>	-13 ≤ h ≤ 13, -17 ≤ k ≤ 14, -18 ≤ l ≤ 15	-17 ≤ h ≤ 17, -16 ≤ k ≤ 14, -12 ≤ l ≤ 11
<b>Reflections collected</b>	11475	9416
<b>Independent reflections</b>	7004 [R <sub>int</sub> = 0.0280]	3545 [R <sub>int</sub> = 0.0664]
<b>Data/restraints/parameters</b>	7004/1/494	3545/0/255
<b>Goodness-of-fit on F<sup>2</sup></b>	1.063	1.175
<b>Final R indexes [I ≥ 2σ (I)]</b>	R <sub>1</sub> = 0.0596, wR <sub>2</sub> = 0.1635	R <sub>1</sub> = 0.1327, wR <sub>2</sub> = 0.3704
<b>Final R indexes [all data]</b>	R <sub>1</sub> = 0.0634, wR <sub>2</sub> = 0.1670	R <sub>1</sub> = 0.1455, wR <sub>2</sub> = 0.3800
<b>Largest diff. peak/hole / e Å<sup>-3</sup></b>	2.90/-0.66	1.73/-1.06

**Table V – 2. Geometric parameters of 2**

<b>Atom</b>	<b>Atom</b>	<b>Length/Å</b>	<b>Atom</b>	<b>Atom</b>	<b>Length/Å</b>
Ni1	N4	1.959(4)	N6	C9	1.498(9)
Ni1	N6	2.044(4)	N7	C10	1.479(5)
Ni1	N7	2.080(3)	N8	C14	1.336(5)
Ni1	O1	2.129(4)	N8	C15	1.353(5)

Ni1	O4	2.145(5)	N9	C15	1.343(5)
Ni1	O3	2.249(4)	N9	C16	1.374(6)
Ni2	N11	1.961(2)	N10	C17	1.339(5)
Ni2	N13	2.048(4)	N10	C16	1.363(6)
Ni2	N14	2.060(5)	N11	C13	1.294(5)
Ni2	O5	2.133(4)	N11	C18	1.338(5)
Ni2	O8	2.157(5)	N12	C16	1.336(5)
Ni2	O7	2.245(4)	N13	C20	1.471(8)
O1	C1	1.298(6)	N14	C21	1.479(6)
O2	C1	1.239(6)	C1	C2	1.509(7)
O3	C6	1.289(7)	C2	C3	1.418(8)
O5	C12	1.294(7)	C3	C8	1.496(7)
O6	C12	1.233(7)	C4	C7	1.414(7)
O7	C17	1.283(6)	C6	C7	1.433(7)
N1	C3	1.334(6)	C9	C11	1.511(9)
N1	C4	1.356(7)	C9	C10	1.512(7)
N2	C4	1.356(6)	C12	C13	1.510(6)
N2	C5	1.359(7)	C13	C14	1.450(7)
N3	C6	1.325(6)	C14	C19	1.489(7)
N3	C5	1.389(7)	C15	C18	1.405(7)
N4	C7	1.308(6)	C17	C18	1.445(7)
N4	C2	1.328(6)	C20	C21	1.514(8)

N5 C5 1.319(7) C20 C22 1.534(9)

Atom	Atom	Atom	Angle/°	Atom	Atom	Atom	Angle/°
N4	Ni1	N6	179.1(3)	O2	C1	O1	123.6(5)
N4	Ni1	N7	94.12(16)	O2	C1	C2	120.8(5)
N6	Ni1	N7	85.0(2)	O1	C1	C2	115.6(4)
N4	Ni1	O1	77.40(16)	N4	C2	C3	118.3(4)
N6	Ni1	O1	102.44(16)	N4	C2	C1	111.5(4)
N7	Ni1	O1	94.25(15)	C3	C2	C1	130.1(5)
N4	Ni1	O4	87.53(18)	N1	C3	C2	121.0(5)
N6	Ni1	O4	93.4(2)	N1	C3	C8	117.3(5)
N7	Ni1	O4	174.81(12)	C2	C3	C8	121.7(4)
O1	Ni1	O4	90.91(18)	N1	C4	N2	122.2(5)
N4	Ni1	O3	77.82(16)	N1	C4	C7	118.4(4)
N6	Ni1	O3	102.32(15)	N2	C4	C7	119.2(5)
N7	Ni1	O3	86.41(14)	N5	C5	N2	116.7(4)
O1	Ni1	O3	155.19(14)	N5	C5	N3	115.2(5)
O4	Ni1	O3	89.13(17)	N2	C5	N3	128.1(5)
N11	Ni2	N13	177.5(2)	O3	C6	N3	122.2(5)
N11	Ni2	N14	93.16(14)	O3	C6	C7	117.4(4)
N13	Ni2	N14	84.4(2)	N3	C6	C7	120.3(5)
N11	Ni2	O5	76.27(11)	N4	C7	C4	121.0(5)
N13	Ni2	O5	104.14(16)	N4	C7	C6	118.6(4)

N14	Ni2	O5	90.9(2)	C4	C7	C6	120.3(4)
N11	Ni2	O8	88.60(14)	N6	C9	C11	113.7(6)
N13	Ni2	O8	93.8(2)	N6	C9	C10	108.7(5)
N14	Ni2	O8	177.88(17)	C11	C9	C10	111.8(6)
O5	Ni2	O8	90.62(19)	N7	C10	C9	108.7(4)
N11	Ni2	O7	79.38(11)	O6	C12	O5	124.0(5)
N13	Ni2	O7	100.19(16)	O6	C12	C13	122.3(5)
N14	Ni2	O7	90.30(18)	O5	C12	C13	113.8(4)
O5	Ni2	O7	155.65(14)	N11	C13	C14	118.6(4)
O8	Ni2	O7	88.87(17)	N11	C13	C12	112.4(4)
C1	O1	Ni1	114.1(3)	C14	C13	C12	128.9(5)
C6	O3	Ni1	108.9(3)	N8	C14	C13	119.9(4)
C12	O5	Ni2	115.0(3)	N8	C14	C19	117.7(4)
C17	O7	Ni2	107.7(3)	C13	C14	C19	122.4(4)
C3	N1	C4	119.6(4)	N9	C15	N8	121.2(4)
C4	N2	C5	116.1(4)	N9	C15	C18	120.2(4)
C6	N3	C5	115.5(5)	N8	C15	C18	118.6(4)
C7	N4	C2	121.5(4)	N12	C16	N10	114.1(4)
C7	N4	Ni1	117.3(3)	N12	C16	N9	117.8(4)
C2	N4	Ni1	121.2(3)	N10	C16	N9	128.2(4)
C9	N6	Ni1	107.8(4)	O7	C17	N10	123.9(4)
C10	N7	Ni1	106.1(3)	O7	C17	C18	119.3(4)

C14	N8	C15	120.3(3)	N10	C17	C18	116.8(4)
C15	N9	C16	115.0(3)	N11	C18	C15	120.7(4)
C17	N10	C16	117.9(3)	N11	C18	C17	117.6(4)
C13	N11	C18	121.9(3)	C15	C18	C17	121.7(4)
C13	N11	Ni2	121.9(2)	N13	C20	C21	108.6(4)
C18	N11	Ni2	115.8(2)	N13	C20	C22	112.3(6)
C20	N13	Ni2	108.4(4)	C21	C20	C22	111.8(6)
C21	N14	Ni2	106.8(3)	N14	C21	C20	108.4(5)

**Table V – 3. Hydrogen Atom Coordinates ( $\text{\AA}\times 10^4$ ) and Isotropic Displacement Parameters ( $\text{\AA}^2\times 10^3$ ) for 2**

Atom	x	y	z	U(eq)
H3	4429	2726	8579	19
H5A	4471	2700	10910	22
H5B	3631	2758	9925	22
H6A	8463	2140	5706	19
H6B	7068	2278	5658	19
H7A	7558	4381	7572	19
H7B	8827	4413	7302	19
H10	10675	10169	1337	16
H12B	11475	10167	37	21

H12C	10648	10189	-954	21
H13A	8023	10794	4296	19
H13B	6660	10575	4300	19
H14A	6329	8491	2404	19
H14B	7752	8534	2712	19
H8A	11206	2378	11580	26
H8B	11651	3262	11005	26
H8C	11818	2157	10690	26
H9	8886	3740	5625	26
H10A	7488	4964	5976	23
H10B	6444	4152	6078	23
H11A	7749	3261	4109	55
H11B	7459	4382	4296	55
H11C	6424	3559	4375	55
H19A	3895	10176	-1623	30
H19B	3419	10876	-885	30
H19C	3307	9715	-798	30
H20	8647	9243	4415	23
H21A	7181	7931	4012	24
H21B	5989	8671	3876	24
H22A	8248	9696	5905	63
H22B	7884	8568	5722	63

**Table V – 4. Geometric parameters of 3**

<b>Atom Atom</b>	<b>Length/Å</b>	<b>Atom Atom</b>	<b>Length/Å</b>
Ni1 N4	1.982(8)	N5 C5	1.347(15)
Ni1 N6	2.081(10)	N6 C9	1.460(16)
Ni1 N7	2.085(9)	N7 C10	1.460(19)
Ni1 O1	2.154(8)	O1 C1	1.324(12)
Ni1 O4	2.183(8)	O2 C1	1.247(13)
Ni1 O3	2.256(7)	O3 C6	1.318(13)
N1 C3	1.320(15)	C1 C2	1.494(15)
N1 C4	1.385(14)	C2 C3	1.461(14)
N2 C4	1.343(14)	C3 C8	1.521(14)
N2 C5	1.389(14)	C4 C7	1.436(14)
N3 C6	1.338(14)	C6 C7	1.466(14)
N3 C5	1.374(14)	C9 C10	1.33(2)
N4 C7	1.320(14)	C10 C11	1.49(2)
N4 C2	1.355(13)		
<b>Atom Atom Atom</b>	<b>Angle/°</b>	<b>Atom Atom Atom</b>	<b>Angle/°</b>
N4 Ni1 N6	94.4(3)	O2 C1 O1	124.7(10)
N4 Ni1 N7	178.0(4)	O2 C1 C2	120.4(9)

N6	Ni1	N7	83.8(4)	O1	C1	C2	114.8(8)
N4	Ni1	O1	76.5(3)	N4	C2	C3	117.2(9)
N6	Ni1	O1	93.0(4)	N4	C2	C1	112.1(8)
N7	Ni1	O1	102.6(3)	C3	C2	C1	130.7(9)
N4	Ni1	O4	88.0(3)	N1	C3	C2	120.7(9)
N6	Ni1	O4	175.4(3)	N1	C3	C8	118.8(9)
N7	Ni1	O4	93.8(3)	C2	C3	C8	120.4(10)
O1	Ni1	O4	91.4(3)	N2	C4	N1	123.8(9)
N4	Ni1	O3	79.3(3)	N2	C4	C7	118.9(9)
N6	Ni1	O3	88.7(4)	N1	C4	C7	117.3(9)
N7	Ni1	O3	101.5(3)	N5	C5	N3	114.6(9)
O1	Ni1	O3	155.8(3)	N5	C5	N2	117.3(9)
O4	Ni1	O3	87.9(3)	N3	C5	N2	128.0(10)
C3	N1	C4	121.4(9)	O3	C6	N3	122.8(9)
C4	N2	C5	116.8(9)	O3	C6	C7	117.9(9)
C6	N3	C5	116.2(9)	N3	C6	C7	119.3(9)
C7	N4	C2	122.3(8)	N4	C7	C4	121.1(9)
C7	N4	Ni1	116.4(6)	N4	C7	C6	118.5(8)
C2	N4	Ni1	121.3(6)	C4	C7	C6	120.2(10)
C9	N6	Ni1	107.7(8)	C10	C9	N6	121.0(14)
C10	N7	Ni1	108.7(8)	C9	C10	N7	118.6(13)
C1	O1	Ni1	114.9(6)	C9	C10	C11	124.4(16)

C6 O3 Ni1 107.9(6) N7 C10 C11 116.9(14)

**Table V- 5. Hydrogen Atom Coordinates ( $\text{\AA}\times 10^4$ ) and Isotropic Displacement Parameters ( $\text{\AA}^2\times 10^3$ ) for 3**

Atom	<i>x</i>	<i>y</i>	<i>z</i>	U(eq)
H6A	7571	2101	5123	55
H6B	7525	2062	3738	55
H7A	9268	4238	4070	54
H7B	9303	4240	5451	54
H8A	3825	3159	1022	69
H8B	4396	4063	676	69
H8C	3508	4231	1278	69
H9A	8995	1799	5507	181
H9B	8943	1742	4031	181
H10	9405	2893	3870	203
H11A	10639	2160	4742	174
H11B	10740	2836	5958	174
H11C	10756	3300	4613	174

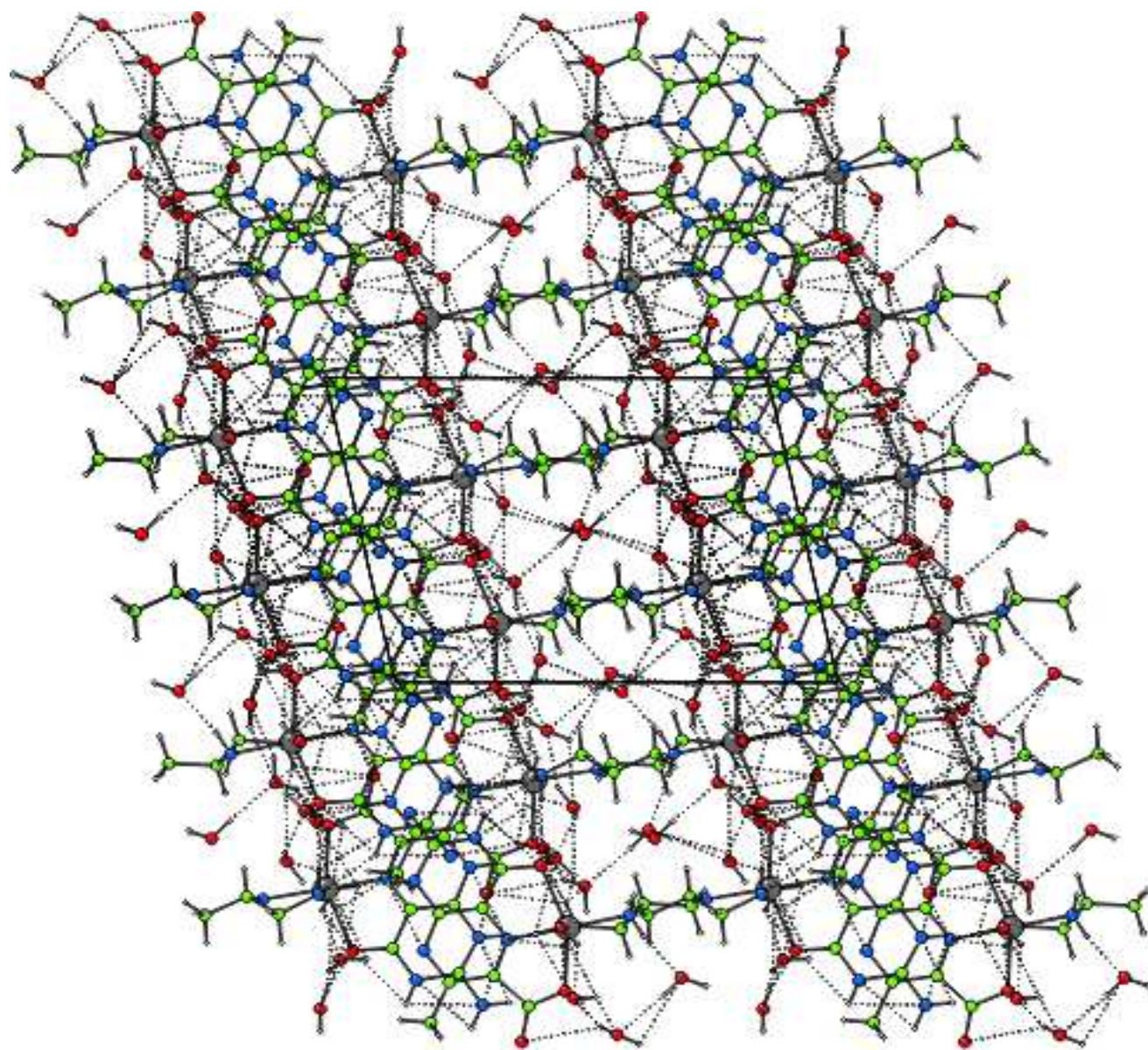


**Figure V-3.** Crystal packing diagram of **2** and H-bonding network viewed along b axis.

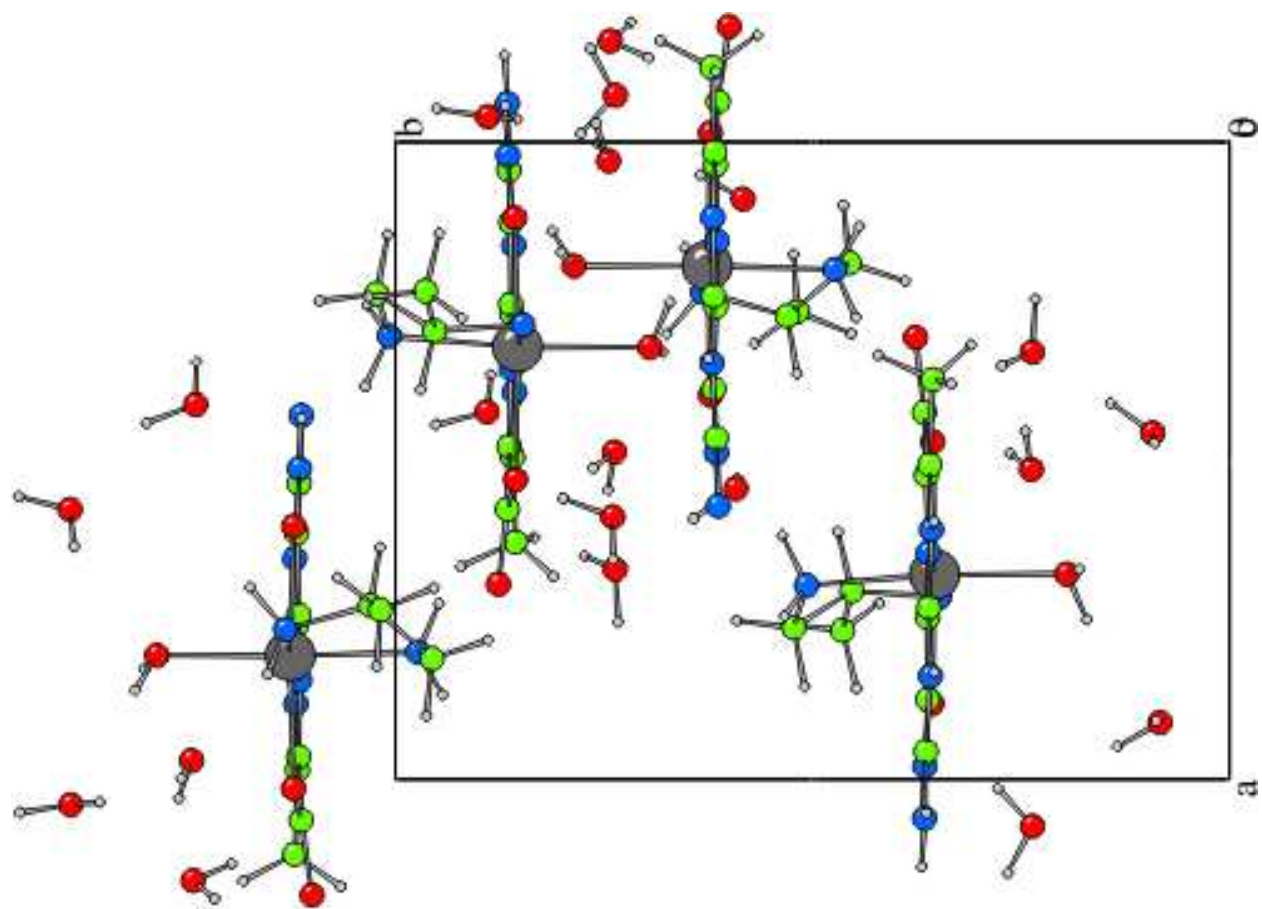


**Figure V – 4.** Unit cell of the complex 2 along c axis

---

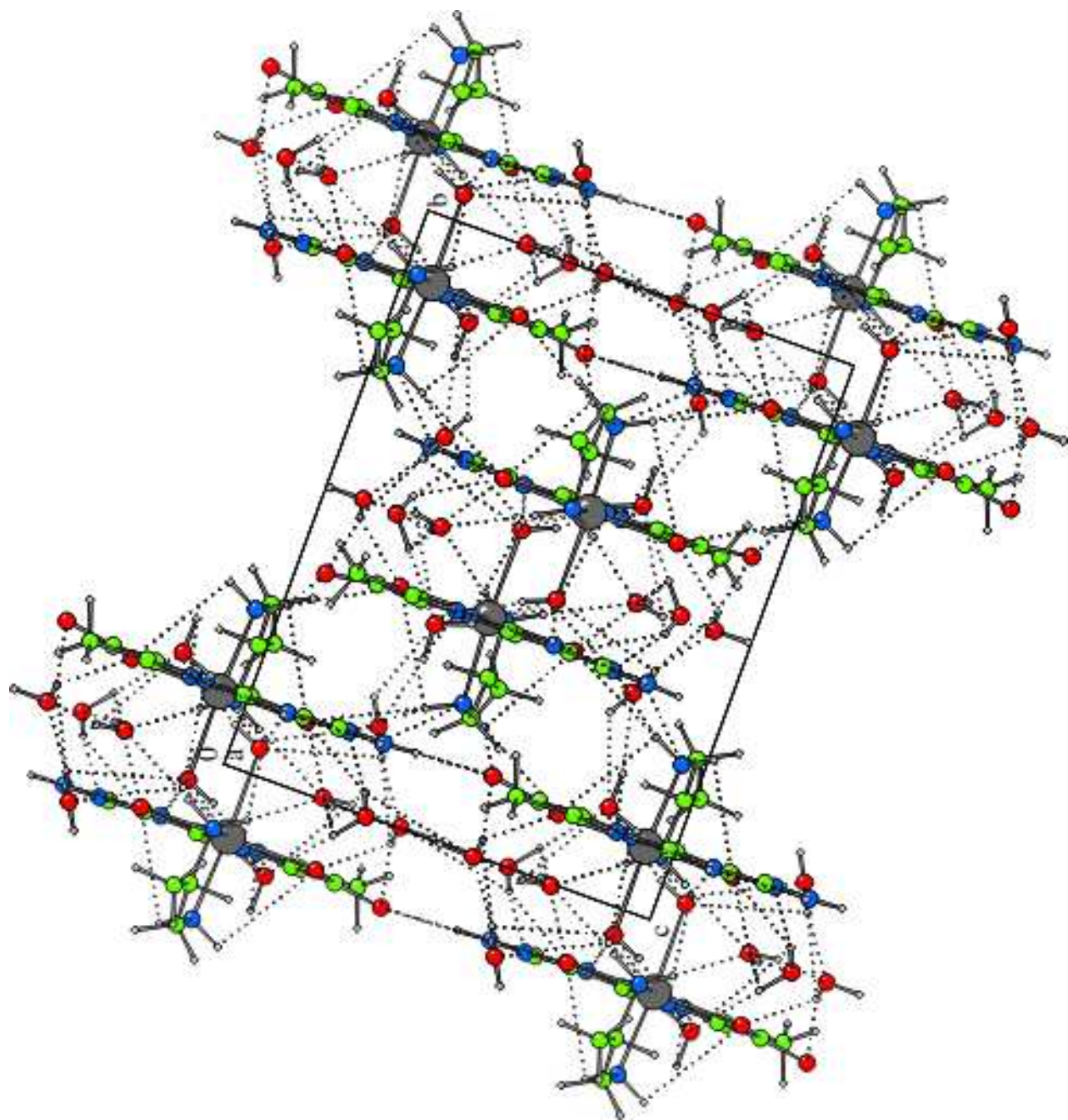


**Figure V – 5.** Crystal packing diagram of **3** and H-bonding network viewed along a axis.

---

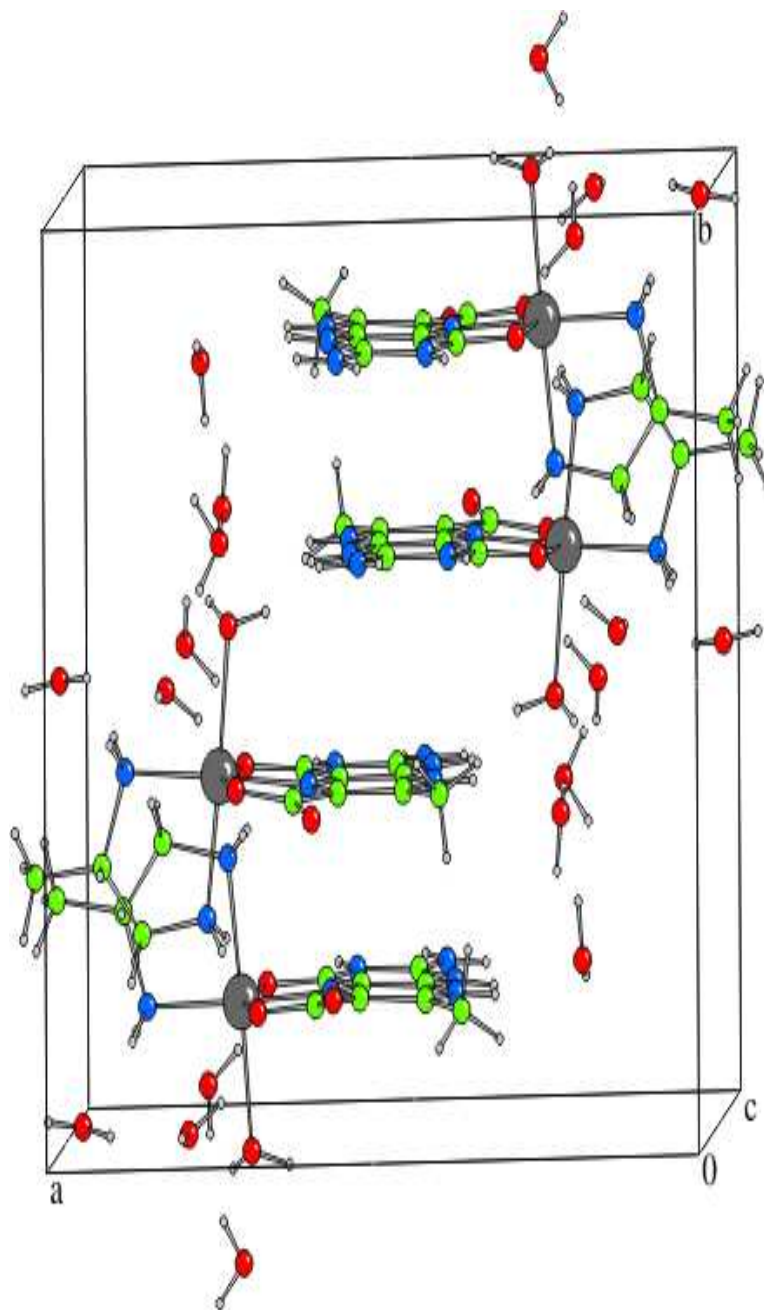


**Figure V – 6.** Unit cell of the complex **3** along *c* axis

---

The Ni(II) atom in **2** is located in a distorted octahedron, where it is coordinated by the tridentate pterin ligand, the bidentate ancillary ligand R-(+)-pn and a water molecule. The pterin ligand forms two five membered chelate rings. The R-(+)-pn chelate ring is arranged orthogonally with

respect to the pterin ligand, for minimising the steric repulsion Figure V-4.<sup>17,18</sup> Geometric parameters of **2** (Table V-2) revealed the extent of departure from octahedral geometry in this case. The basal plane is formed by the two nitrogen atoms (N6, N7) of R-(+)-pn, the pyrazine ring nitrogen atom (N4) and the aquo group atom (O4). The axial positions are occupied by the two pterin oxygen atoms (O1 and O3) with the latter one forming the longest axial bond [2.249(4)Å]. Considering the charge balance of this complex, it is apparent that the pterin ligand is acting as a bidentate O – N – O donor. Of the three axes, least deviation from linearity is observed for the N4 – Ni1 – N6 axis [179.1(3)°], where the highest electron density is concentrated [Ni – N4: 1.959(4)Å; Ni – N6 : 2.044(4)Å]. This situation represents contributions from the  $\sigma$ -donor atom N6 (pn) and the N4 atom of the redox non-innocent pterin ligand from the opposite directions of the Ni(II) centre ( $d^8$ ), with possible assistance from the  $\pi$ -donating phenolate and carboxylate oxygen atoms<sup>18</sup>.

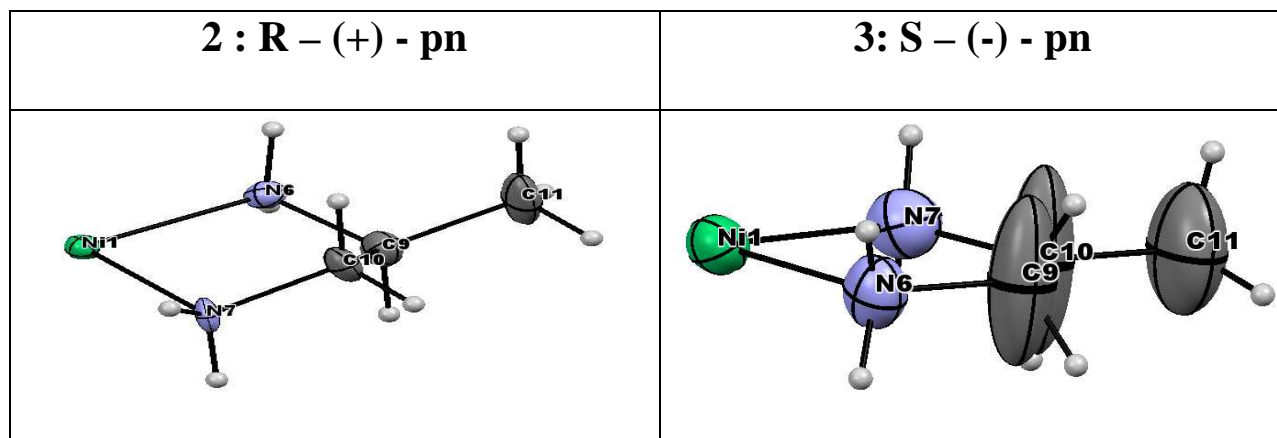
The exocyclic bond length data of the pyrimidine ring, e.g., C6 – O3 [1.289(7)Å] and C5 – N5 [1.319(7)Å] merit attention. Their near double bond character is ascribed to the electron shuffling process by the pterin moiety, from the pyrazine ring nitrogen atom (N1) to the C6-carbonyl group, during formation of the Ni1 – O3 bond.<sup>22,23</sup> In the crystal N – H...O, O – H ...N and O – H ...O hydrogen bonds link the complex molecule and lattice water molecule into layers along the b axis (Figure V-3). The lattice water molecules are decisive for crystal packing.

The molecular structure of **3** (Figure V-2) also conform to a distorted octahedral geometry, as evident from the geometric parameters in Table V-4. A major cause of such distortion from regular geometry is mainly due to the formation of two five membered chelate rings by the pterin ligand with small bite angles [87.9° and 76.5°(3)] for minimising the steric repulsion. The pterin ring and the pn ring are arranged orthogonally (Figure V-6). As earlier,

least deviation [ $178.0(4)^\circ$ ] from linearity is observed along the N4 – Ni – N7 axis. The exocyclic bonds of the pyrimidine ring namely C6 – O3 [ $1.318(13)\text{\AA}$ ] and C5 – N5 [ $1.347(15)\text{\AA}$ ] show near double bond character as well. The crystal packing diagram of **3** is shown in Figure V-5.

A persual of Figure V-3 and V-5 shows extensive differences in H-bonding pattern between them; this may be traced partly to the conformational difference associated with the R-(+)-pn and S-(-)-pn chelate rings as summarised below.

Figure V-7 shows the conformational differences with respect to the “pn” chelate rings, between **2** and **3**. A comparison of the projections with that in Scheme IV-10, indicates  $\delta$ -conformation in each case.<sup>79,90,149</sup> But their extent of puckering of the ‘pn’ chelate ring is different, with that for **3** [S-(-)-pn] approaching near planarity. Achieving equatorial disposition of the CH<sub>3</sub> – group (of ‘pn’ chelate ring) appears to be the main driving force behind such an observation.<sup>79,90</sup> Such conformational differences gives rise to subtle difference in the CD spectra of **2** and **3** as discussed later.



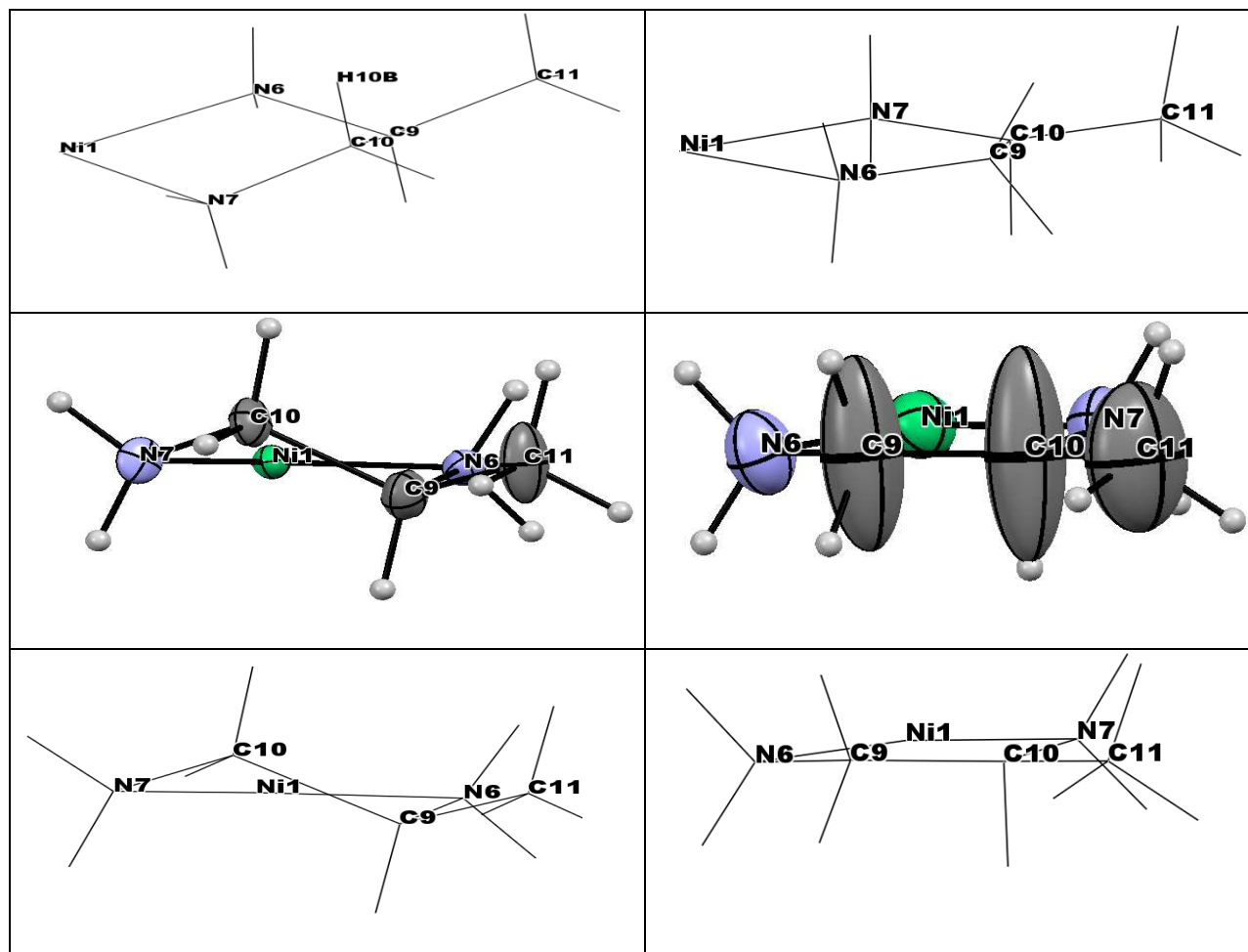


**Figure V-7.** Projections of x-ray structural data of **2** and **3** for viewing the puckering of R-(+)-pn/S-(-)-pn [pn = 1,2-diaminopropane] chelate rings respectively, from different angles.<sup>79,90</sup> For **2** [with R-(+)-pn] a  $\delta$ -conformation is observed, while in case of **3** [with S-(-)-pn], the chelate ring approach planarity for achieving the equatorial disposition of the CH<sub>3</sub> group.

## ESIMS DATA of **2**

The molecular ion peak at m/z 458 corresponds to the species  $[M-2H]^+$ , relative abundance=20%; the peak at m/z 352 corresponds to the dehydrated species  $[M-6H_2O]^+$ , relative abundance=65% and that m/z 702 is due to the dimer of the dehydrated species  $2[M-6H_2O-H]$ , relative abundance=100% ; all the isotope distribution patterns could be simulated, where M represents to the corresponding molecular formula of **2** ( $NiC_{11}H_{27}N_7O_9$ , FW 459.71)

The above data indicate stability of the Ni(II) – pterin as well as the Ni(II) – pn bonds, which remains intact during the above mass spectral process. Figures V-8 and V-10 show the relevant data.

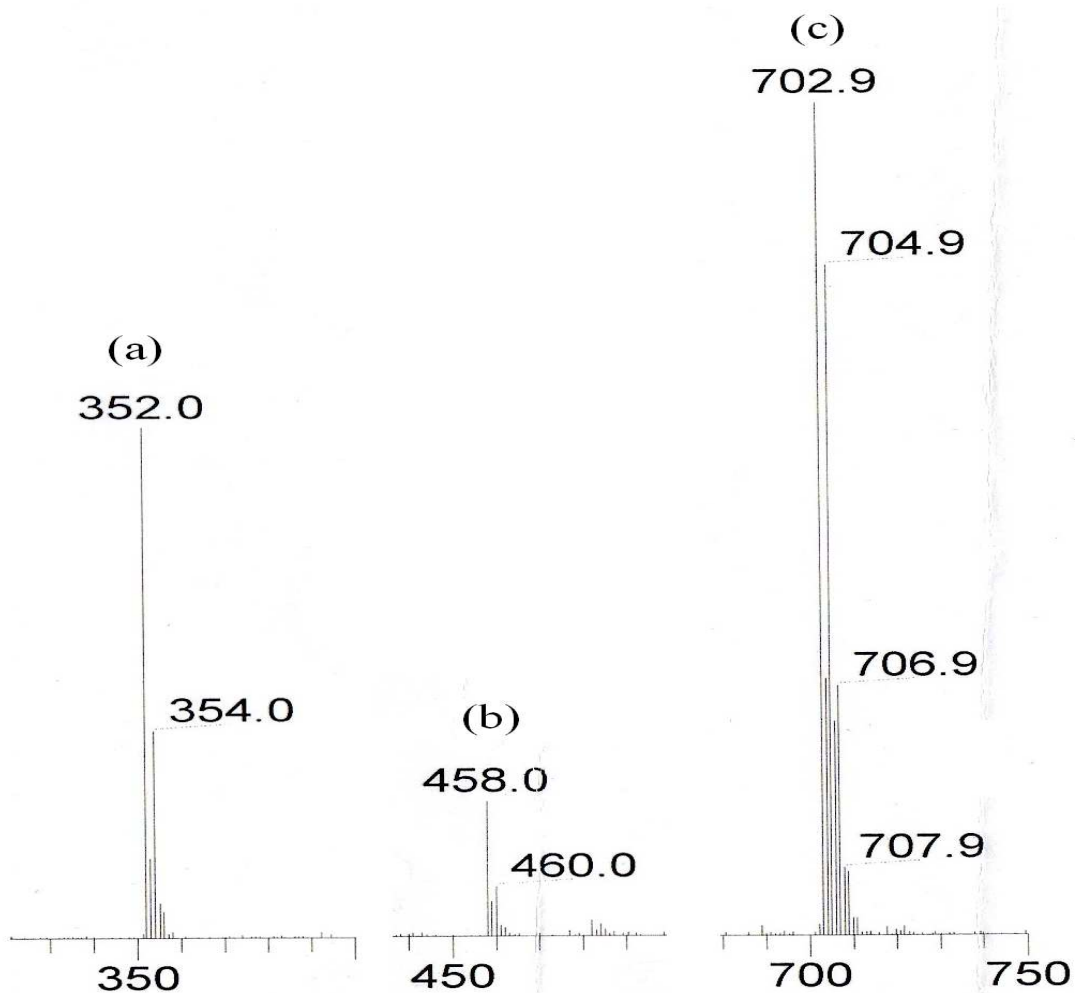


**Figure V-8.** ESIMS data of **2**: (a) for the peak at  $m/z = 352$  corresponding to the fragment  $[M-6H_2O]^+$ , relative abundance=65%; (b)  $m/z = 458$  for the peak corresponding to the fragment  $[M-2H]^+$ , relative abundance=20%; (c)  $m/z = 702$  for the peak corresponding to the fragment  $2[M-6H_2O-H]^+$ , relative abundance=100%. Here M is the molecular formula of **2**.

---

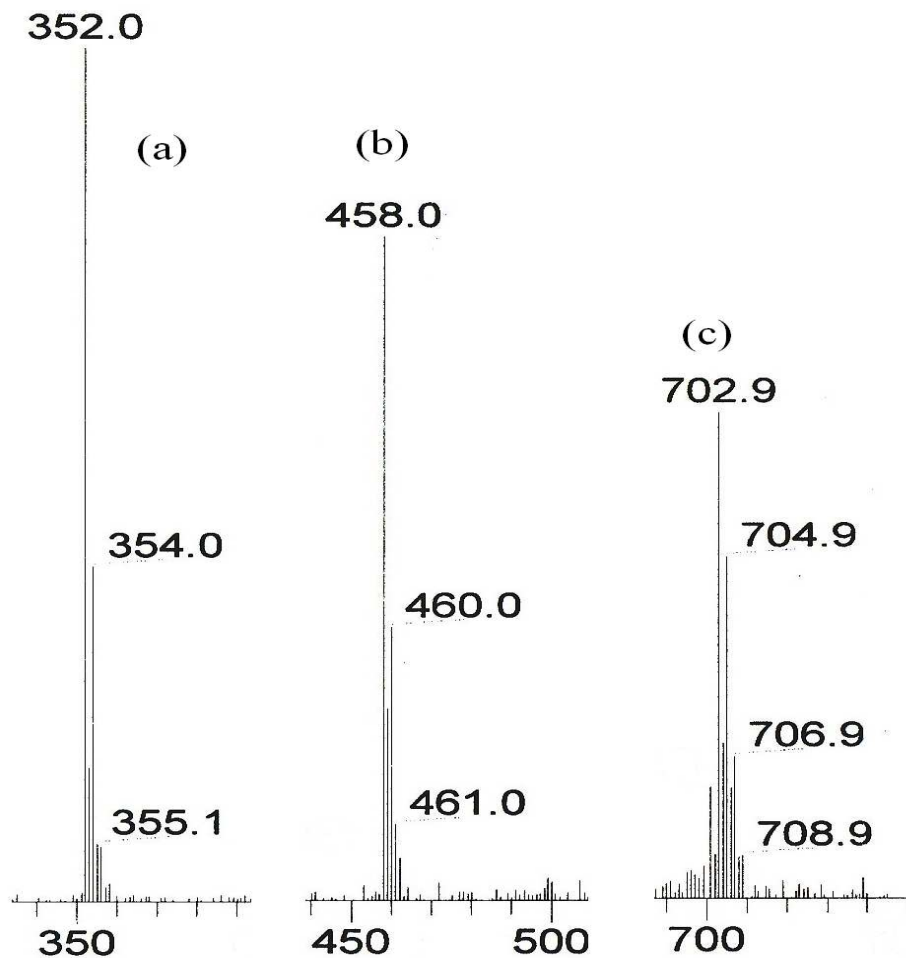


**Figure V-9.** ESIMS data of **3**: (a) for the peak at  $m/z = 352$  corresponding to the fragment  $[M-6H_2O]^+$ , relative abundance= 100%; (b)  $m/z = 458$  for the peak corresponding to the fragment  $[M-2H]^+$ , relative abundance= 83%; (c)  $m/z = 702$  for the peak corresponding to the fragment  $2[M-6H_2O-H]^+$ , relative abundance= 62%. Here M represents the formula of **3**.

---

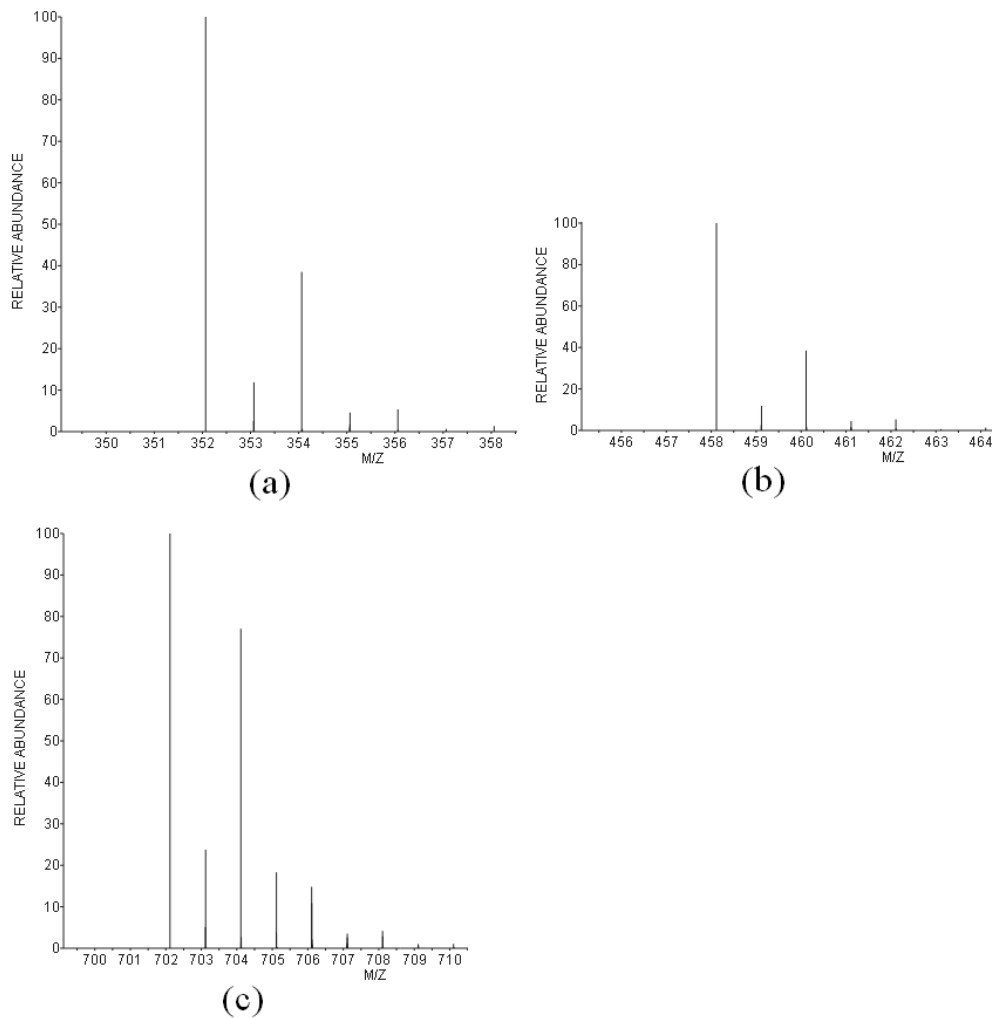


**Figure V-10.** The calculated isotope patterns of **2** & **3**: (a) for the peak at  $m/z = 352$  corresponding to the fragment  $[M-6H_2O]^+$ ; (b)  $m/z = 458$  for the peak corresponding to the fragment  $[M-2H]^+$ ; (c)  $m/z = 702$  for the peak corresponding to the fragment  $2[M-6H_2O-H]^+$ . Here M has the usual meaning.

### ESIMS DATA of **3**

The molecular ion peak at  $m/z$  458 corresponds to the species  $[M-2H]^+$ , relative abundance= 83%; the peak at  $m/z$  352 corresponds to the dehydrated species  $[M-6H_2O]^+$ , relative abundance= 100% and that at  $m/z$  702.9 is due to the dimer of the dehydrated species  $2[M-6H_2O-H]$ , relative abundance= 62%; all the isotope distribution patterns could be simulated, where M represents the corresponding molecular formula of **3** (same as that of **2**; Figure V-9 and V-10). Once again the stability of metal-ligand bonds of **3** is indicated, remaining essentially intact during the mass spectral process.

Taken together with the microanalytical and x-ray structural data, such ESIMS data affirm the chemical compositions of **2** and **3**, as spelt out in the earlier sections as well as their purity. Finally, a comparison of Figures V-8 and V-9 underlines an interesting aspect; although the three above-mentioned peaks are similar with respect to their positions ( $m/z$  values), their relative intensities (relative abundance) are different, most likely originating from the differences in the unit cell structures of **2** and **3** as well as their H-bonding patterns (Table V-1; Figure V-3 to V-6).

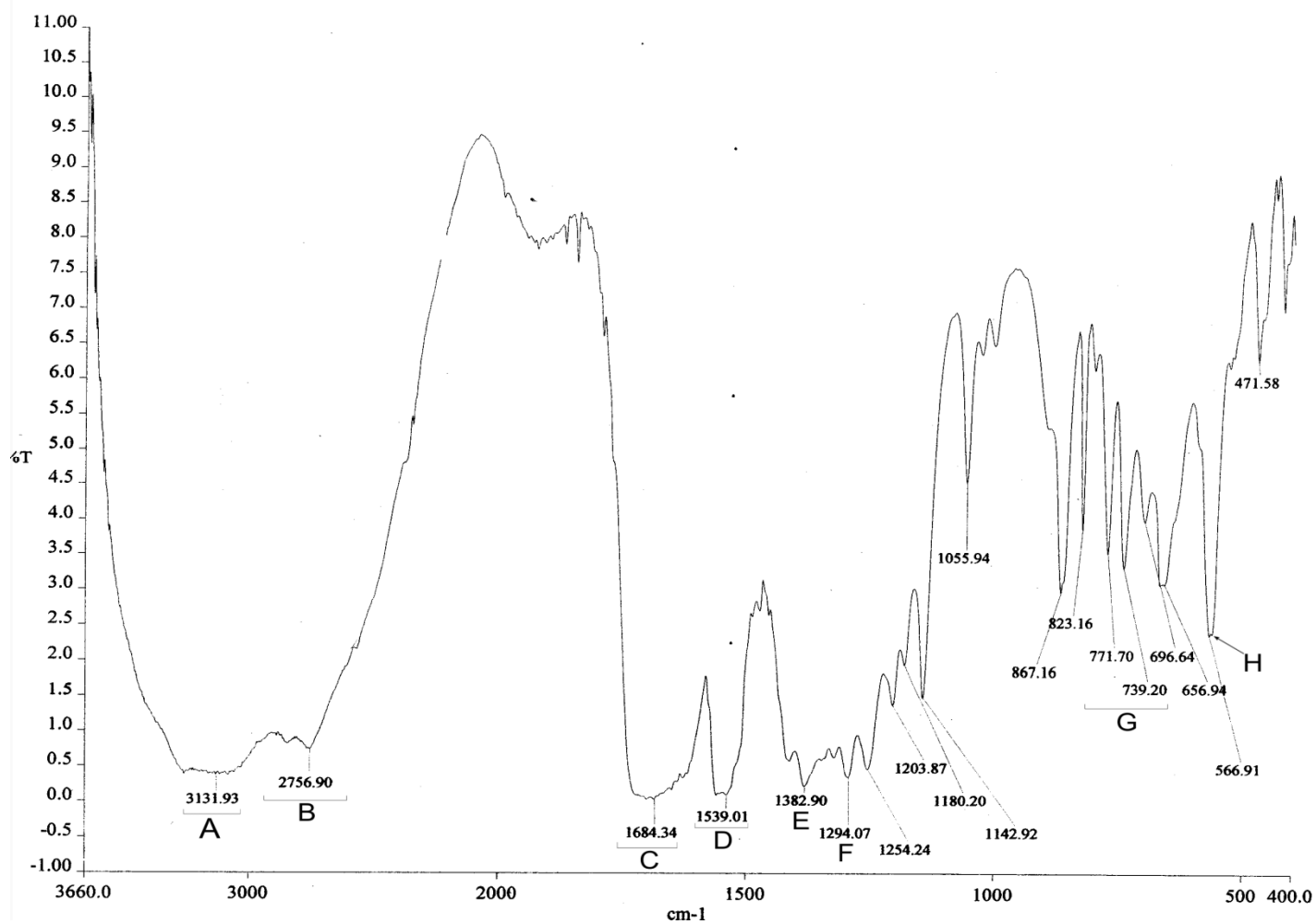


**Figure V-11.** IR spectrum (KBr) of H<sub>2</sub>L · 1.5H<sub>2</sub>O (**1**)

- A: the broad band over the region 3250-3050 cm<sup>-1</sup> due to the  $\nu(\text{OH})$  and  $\nu(\text{NH})$  stretching vibrations of the hydrogen bonded H<sub>2</sub>O, -COOH(6), NH(3) and NH<sub>2</sub>(2) groups, Scheme III-1;
- B: the  $\nu(\text{CH})$  stretching vibrations of the CH<sub>3</sub>(7) group are observed at 2851 cm<sup>-1</sup> and 2757 cm<sup>-1</sup> respectively;

- C: an intense broad band centred at  $1684\text{ cm}^{-1}$  and spread over the region  $1718\text{-}1636\text{ cm}^{-1}$  is due to the  $\nu(\text{C}=\text{O})$  modes of the  $\text{C}=\text{O}(4)$  and  $\text{COOH}(6)$  groups, (Scheme III-1); the N-H bending vibrations of the  $\text{NH}_2(2)$  group are occluded under this band;
- D: the  $\nu(\text{C}=\text{C})$  and  $\nu(\text{C}=\text{N})$  modes at the pterin ring appears around  $1560\text{-}1539\text{ cm}^{-1}$ ;
- E&F: the  $\delta(\text{O-H})$  and  $\nu(\text{C-O}) + \delta(\text{O-H})$  modes of the  $\text{COOH}(6)$  group appear at  $1382\text{ cm}^{-1}$  and  $1294\text{ cm}^{-1}$  respectively;
- G: different types of skeletal bending vibrations of the pterin ring appear over the region  $860\text{-}650\text{ cm}^{-1}$ ;
- H: rocking vibrations of the  $\text{NH}_2(2)$  group appears around  $567\text{ cm}^{-1}$ .
-

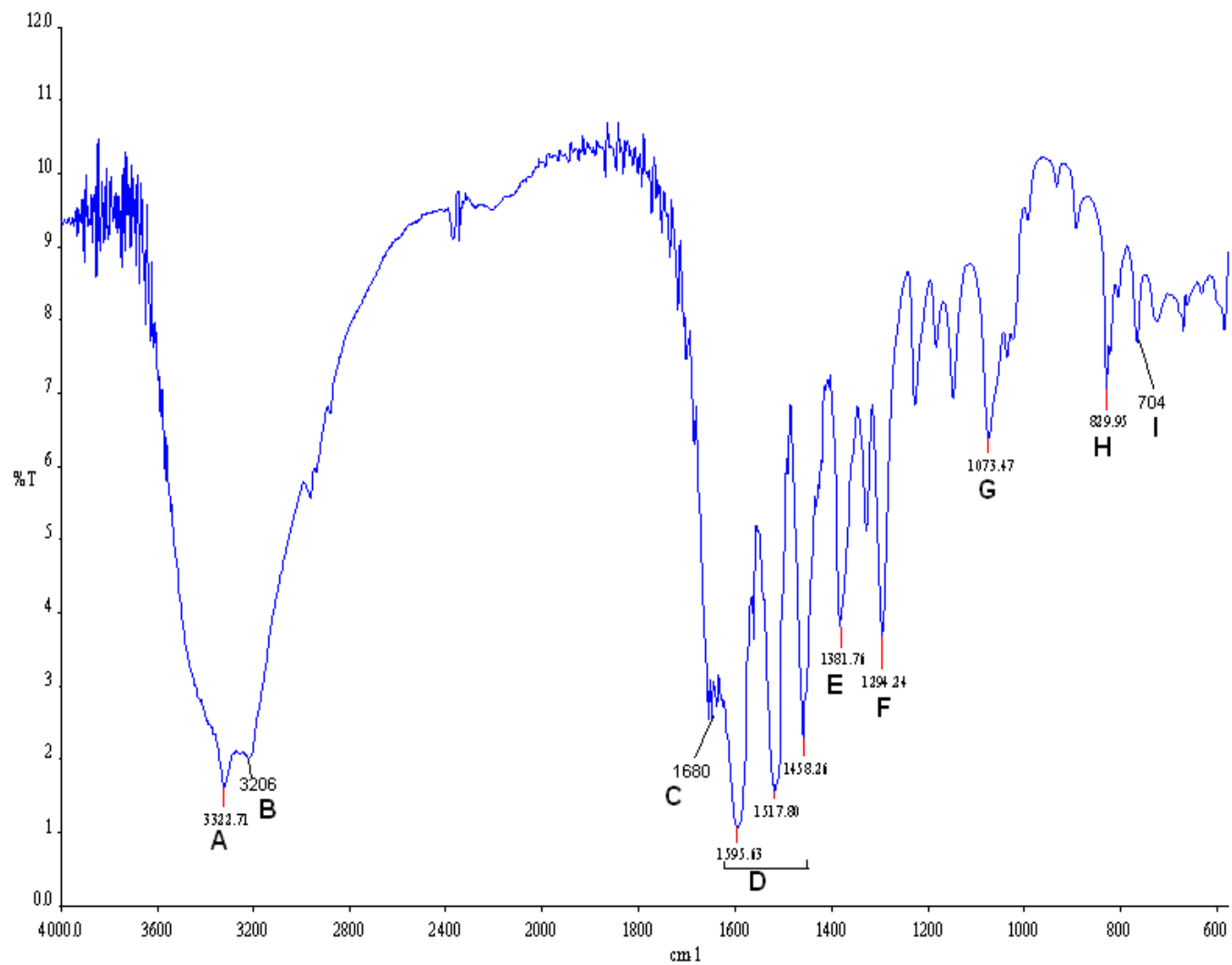
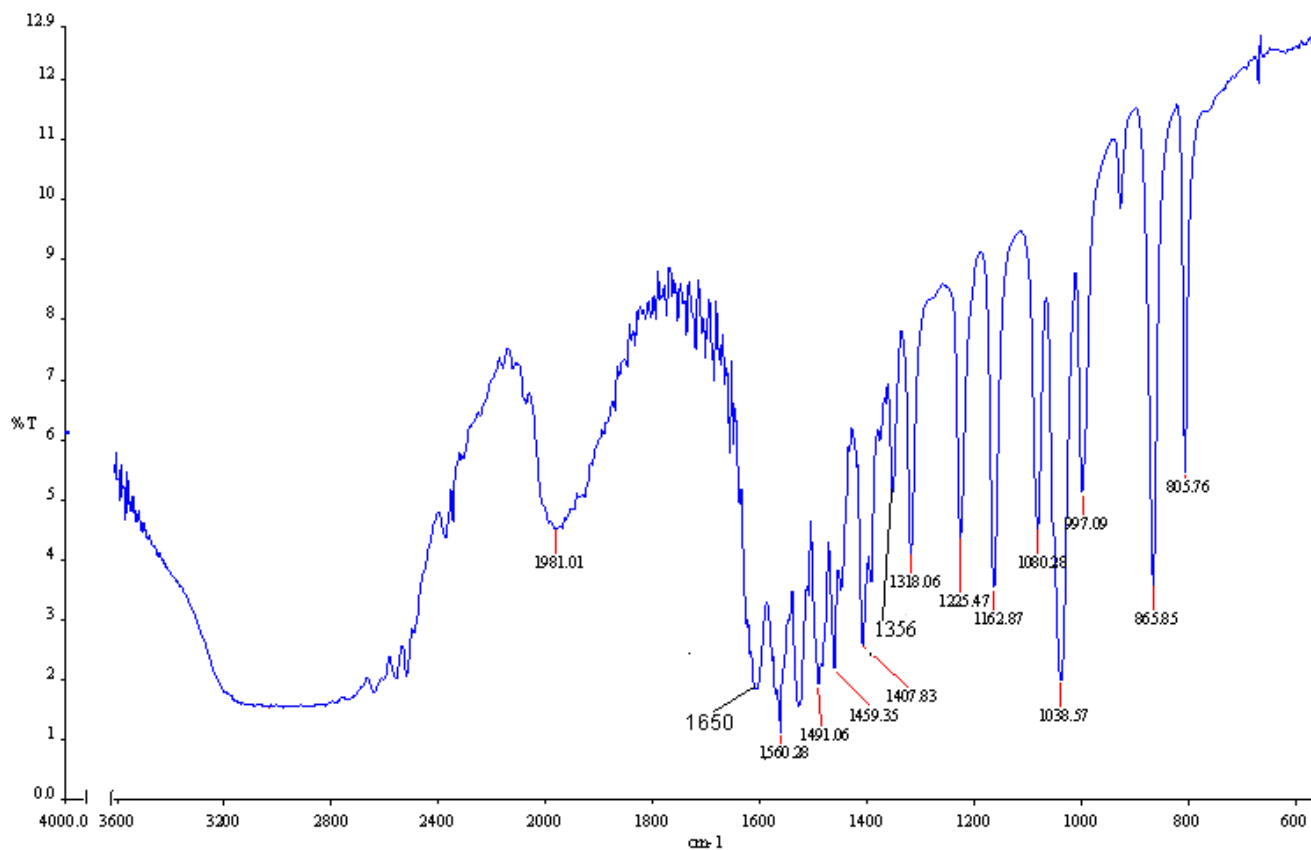


**Figure V-12.** IR spectrum (KBr) of **2**



. **Figure V-13.** IR spectrum (KBr) of **3**

**IR Spectroscopy.** The IR spectrum of the pterin ligand ( $\text{H}_2\text{L} \cdot 1.5\text{H}_2\text{O}$ , **1**) is shown in Figure V-11, while those of **2** and **3** are shown in Figure V-12 and V-13 respectively. As pointed out in the earlier chapters, the intense broad band over the region  $3300 - 2500 \text{ cm}^{-1}$  (Figure V-11) originate from the  $\nu(\text{OH})$ ,  $\nu(\text{NH})$ ,  $\nu(\text{CH})$  stretching vibrations of the different functional groups of **1** as well as its lattice water molecules; another intense broad band centred around  $1684 \text{ cm}^{-1}$  corresponds to the  $\nu(\text{C}=\text{O})$  modes of the  $\text{C}=\text{O}(4)$  group as well as that of the  $\text{COOH}(6)$  functional groups of **1**.<sup>21,148</sup> Few  $\nu(\text{C}=\text{C})$  and  $\nu(\text{C}=\text{N})$  vibrations of the pterin ring appear around  $1560\text{-}1539 \text{ cm}^{-1}$ . Two other broad bands at  $1383 \text{ cm}^{-1}$  and  $1294 \text{ cm}^{-1}$  characterize the  $\delta(\text{O}-$

H) and  $\nu(\text{C-O}) + \delta(\text{O-H})$  modes of the  $\text{COOH}(6)$  group.<sup>21</sup> It is evident from Figures V-12 and V-13 that most of the above-mentioned IR bands are modified on complex formation with the Ni(II) centre in **2** and **3**, through deprotonation of the  $\text{COOH}(6)$  and  $\text{NH}(3)$  groups (Scheme V-1); their broad bands centred around  $3300 - 3200 \text{ cm}^{-1}$  correspond to the extra- and intraspheric water molecules [ $\nu(\text{OH})$ ] and the  $\text{NH}_2(2)$  group [ $\nu(\text{NH})$ ]. The  $\nu_{\text{as}}$  and  $\nu_{\text{s}}$  stretching vibrations of the  $\text{CO}_2'$  group appear at  $1659 - 1650 \text{ cm}^{-1}$  and  $1382 - 1356 \text{ cm}^{-1}$  respectively; the  $\Delta\nu$  values ( $294 - 278 \text{ cm}^{-1}$ ) indicate unidentate carboxylate coordination, in accordance with their x-ray structural data (Figure V-1 and V-2).<sup>87,88</sup> The  $\text{NH}_2$  deformation vibrations (of the 'pn' chelate ring) contribute to the broad nature of the IR bands around  $1600 \text{ cm}^{-1}$  for both **2** and **3**. Finally, a comment is necessary about the difference in relative intensity of peaks around  $1700 - 750 \text{ cm}^{-1}$  region of **2** and **3**, although their numbers are almost the same. One likely reason is their difference in hydrogen bonding patterns (Figure V-3 and V-5); the more intense bands at  $865 \text{ cm}^{-1}$  for **3** (Figure V-13) arise most likely from the out-of-plane C - H deformation vibrations of the  $\text{CH}_3$  group [of the S(-)-pn ring].<sup>21,148</sup> The greater distortion of the aforesaid 'pn' ring [Figure V-7] is another possible reason of such an observation.

**Fluorescence emission spectra.** Fluorescence emission spectra of **2** and **3** in  $\text{CH}_3\text{OH}$  are shown in Figure V-14 and V-15 respectively. The reduced forms of these complexes (**2R** and **3R**) were also studied by the addition of requisite quantity of  $\text{NaBH}_4$  to the methanolic solutions of **2** and

3. As discussed in chapter IV, such reduced forms are the corresponding Ni(I) complex with the 7,8-dihydro forms of the pterin ligand ( $L^{2-}$ , Scheme IV-6).

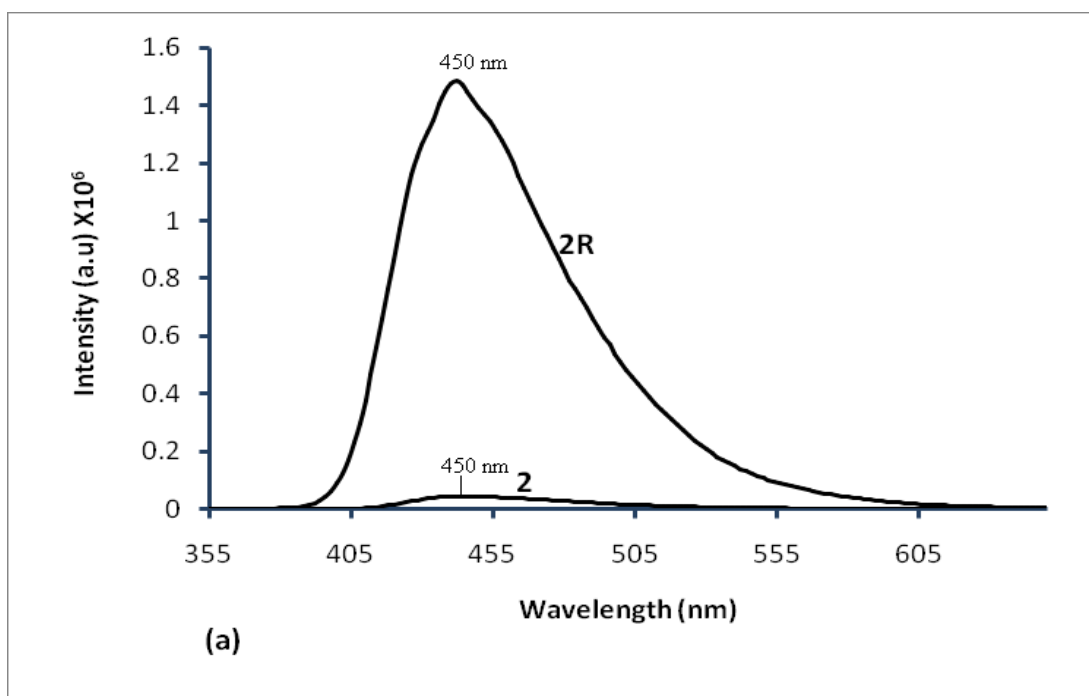


**Figure V-14.** Fluorescence emission spectra of **2** ( $\text{CH}_3\text{OH}$ ,  $1.1 \times 10^{-3}$  M), **2R** ( $\text{CH}_3\text{OH}$ ,  $1.4 \times 10^{-3}$  M).

---

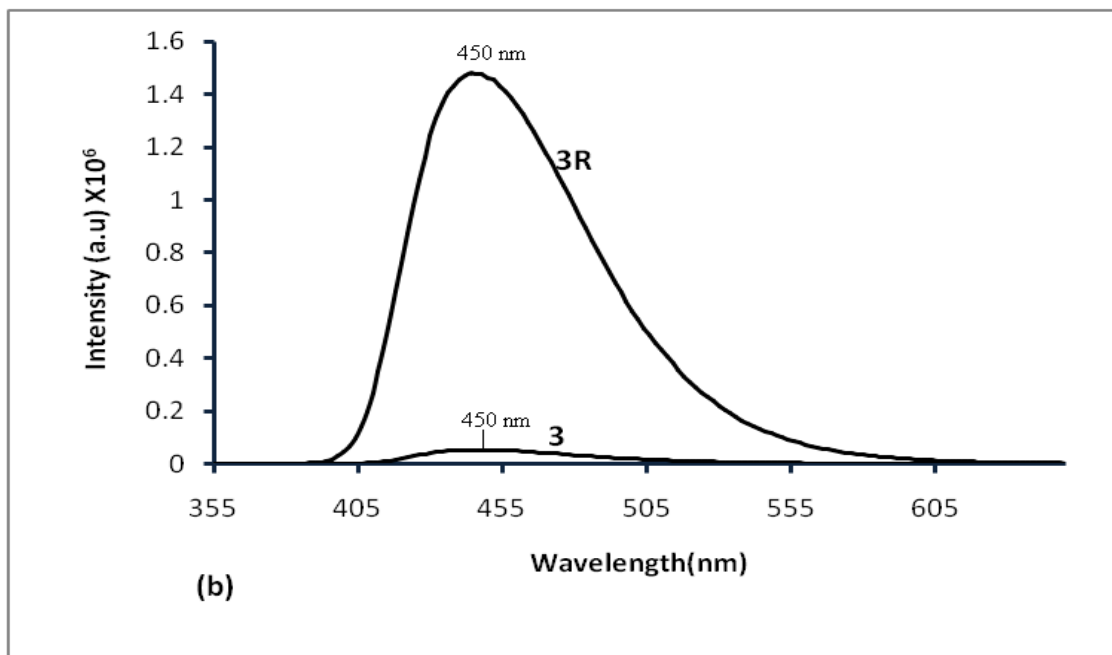
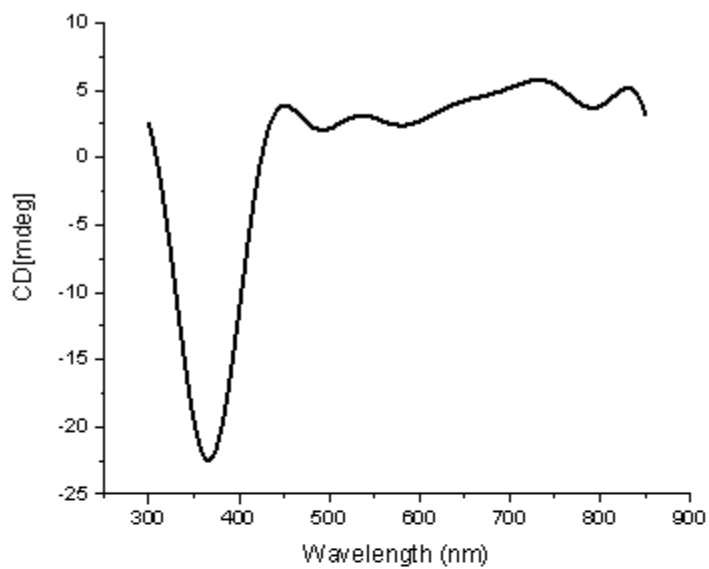
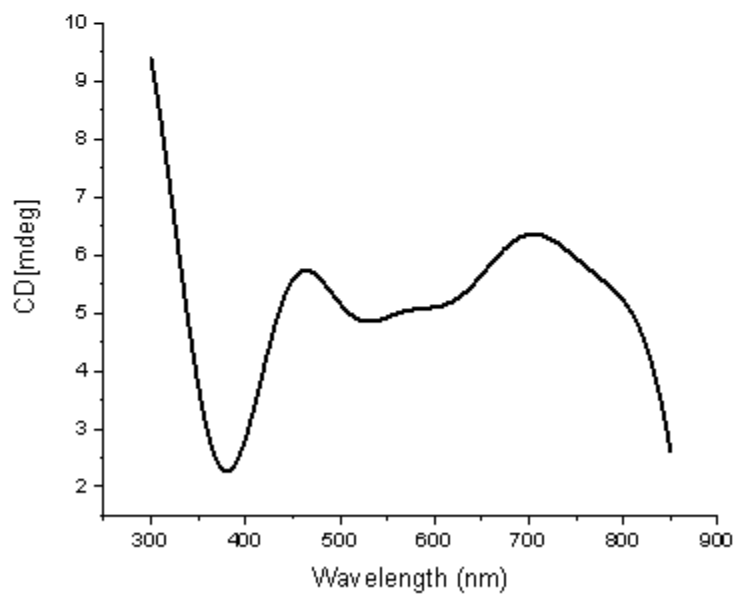


**Figure V-15.** Fluorescence emission spectra of **3** ( $\text{CH}_3\text{OH}$ ,  $5.8 \times 10^{-4}$  M), **3R** ( $\text{CH}_3\text{OH}$ ,  $5.8 \times 10^{-4}$  M).

Although the emission maximum appears consistently at 450 nm in all these cases, a considerable enhancement of fluorescence intensity is observed upon  $\text{NaBH}_4$  reduction. This can be associated with the greater electronic circulation in the rigid reduced complex molecules, involving the extended  $\pi$  orbitals (pterin) and Ni(I) ( $d^9$ ) orbitals; there appears to be less scope for the loss of the vibronic energy.<sup>36</sup> MLCT type transitions [ $\text{Ni(I)}e_g^* \rightarrow \pi^*$ , pterin] are also possible.<sup>32</sup>



(a)



(b)

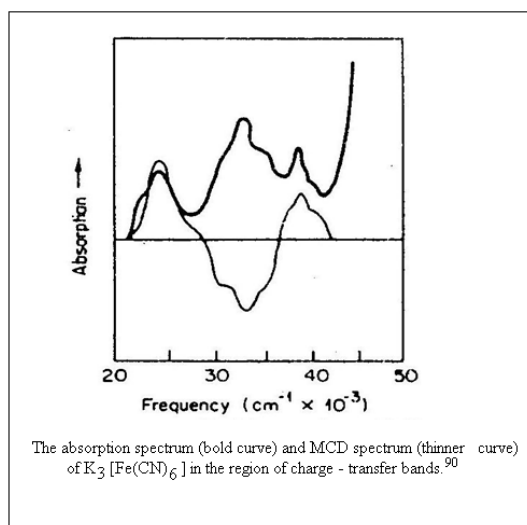
**Figure V-16.** CD spectral data in CH<sub>3</sub>OH of (a) **2** ( $1.3 \times 10^{-3}$  M); (b) **3** ( $1.1 \times 10^{-3}$  M).

## Circular Dichroism Spectroscopy

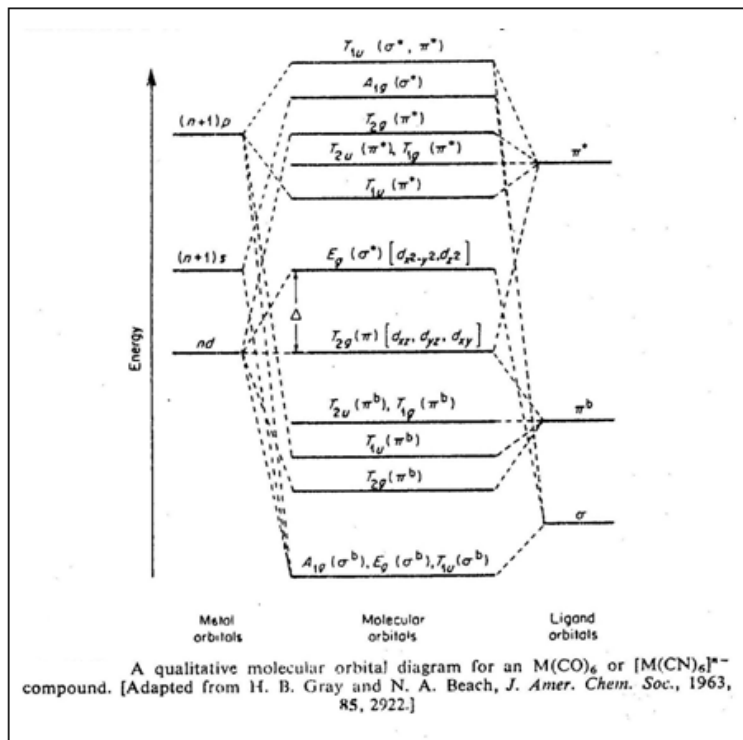
The CD spectral data of **2** and **3** are shown in Figure V-16. The two above spectra can be subdivided into two distinct regions:

1. 300 – 450 nm region, where the LMCT type transition occurs, characterized by a distinct negative Cotton effect; on the basis of MCD spectral study of  $K_3[Fe(CN)_6]$ , such a negative CD band is assigned to a  $t_{2u}$  (ligand  $\pi$  orbital)  $\rightarrow$   $t_{2g}$  (metal) transition (Scheme V-6);<sup>90, 150-152</sup>
2. 450 – 850 nm region where a series of weak positive Cotton effects are observed, corresponding to the different spin-allowed and spin-forbidden transitions of the Ni(II) centre (Scheme IV-7 and IV-8).

The  $\delta$ -conformation of the 'pn' chelate ring (Figure V-7), decides the positive nature of the Cotton effects of the second type.<sup>149</sup> The greater puckering of the 'pn' chelate ring is possibly responsible for the higher intensity of such bands for **3**.



**Scheme V-6(a)**



Scheme V – 6(b)

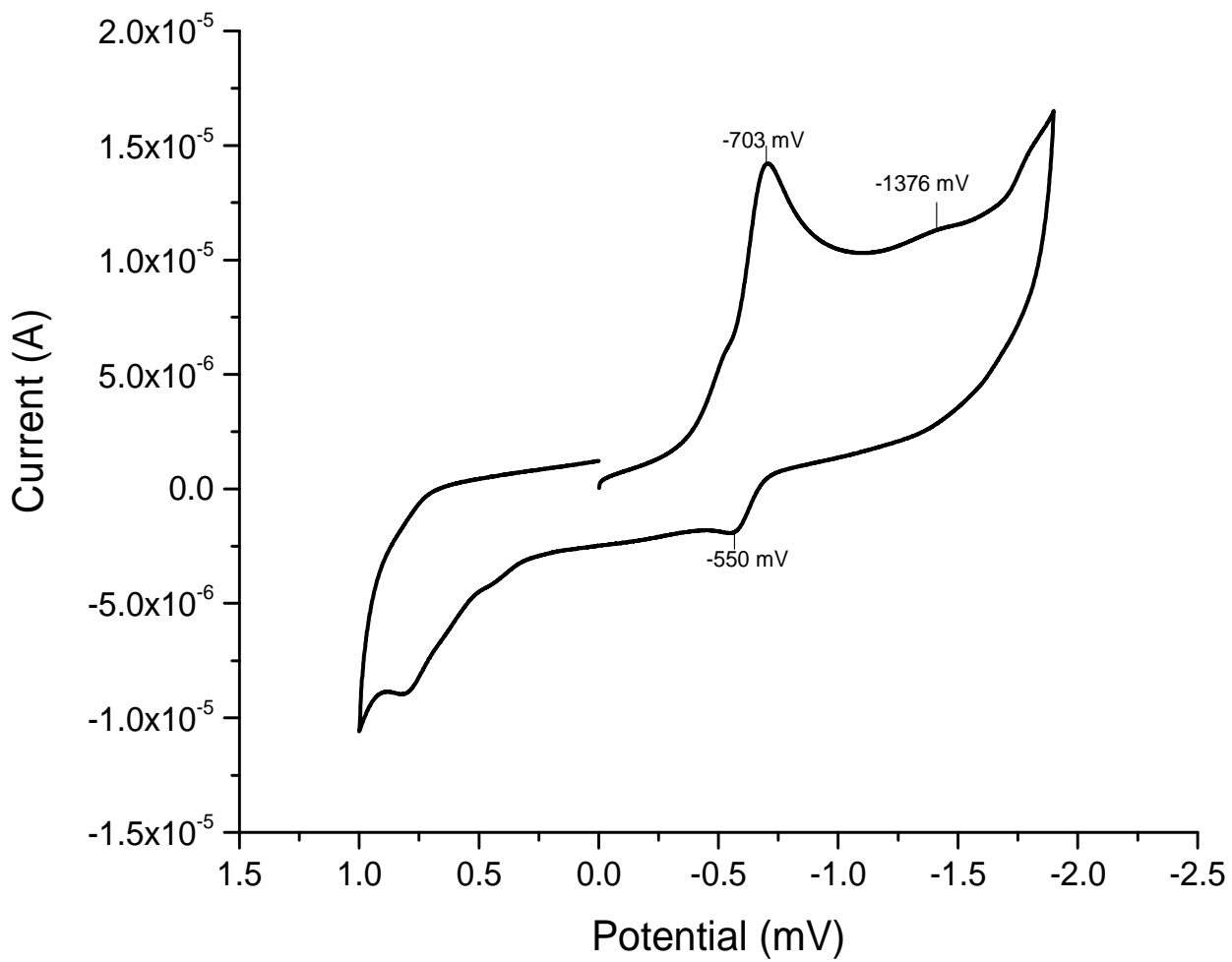


**Figure V- 17.** Cyclic voltammetry data of **2** in DMSO ( 0.1M TBAP; scan rate,  $100\text{mV s}^{-1}$ ).

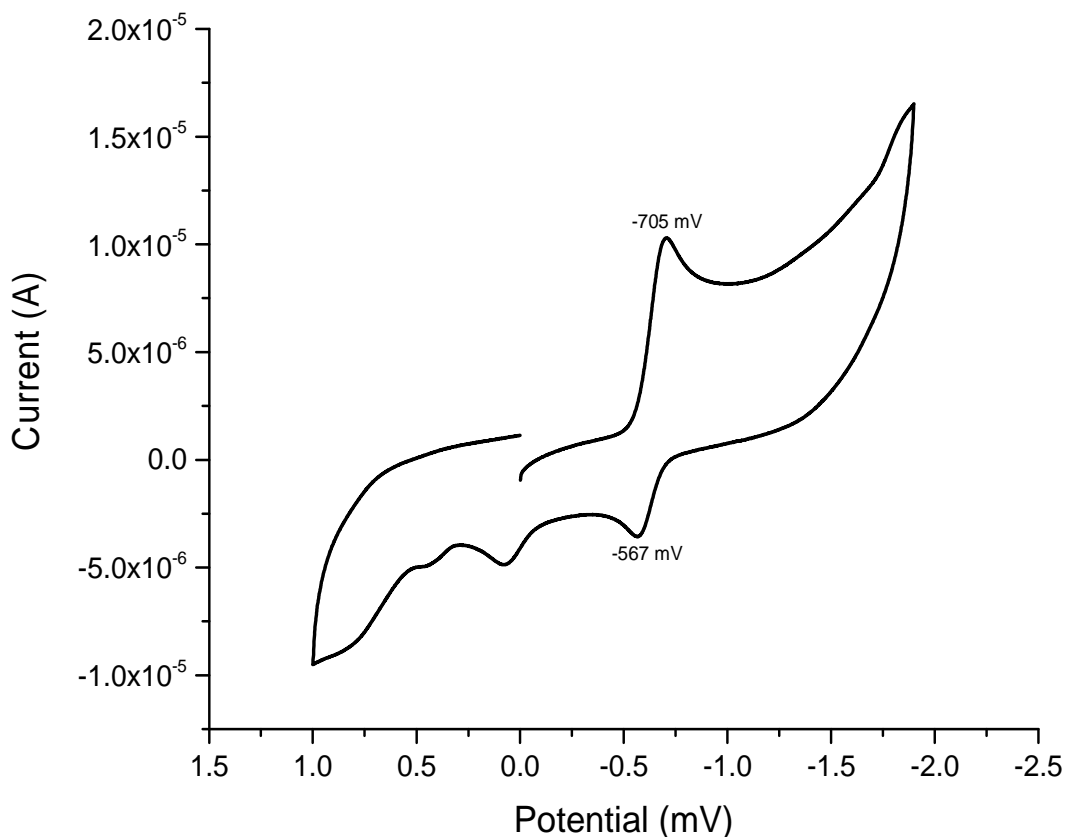


**Figure V - 18.** Cyclic voltammetry data of **3** in DMSO ( 0.1M TBAP; scan rate, 100mV s<sup>-1</sup>).

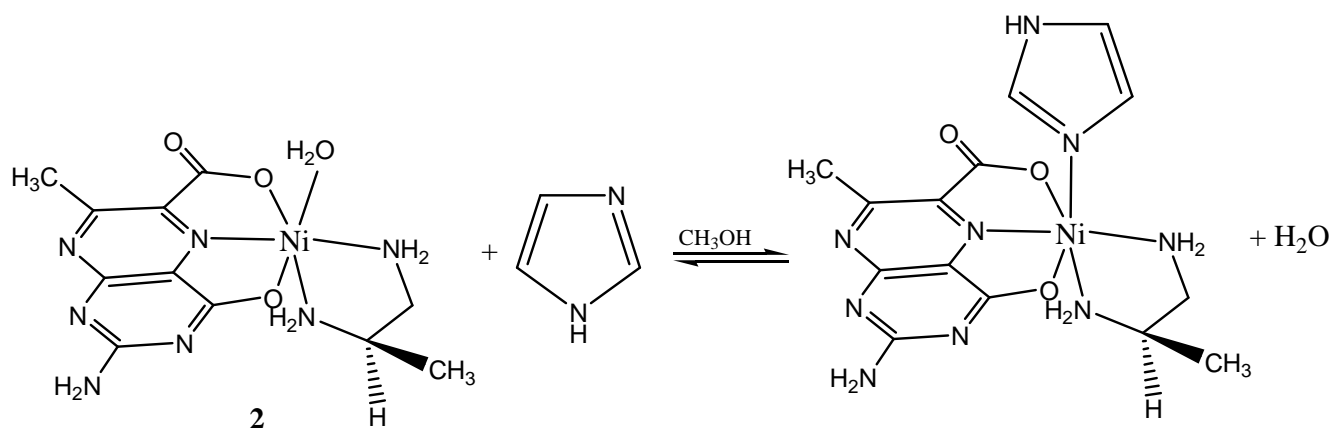
### Cyclic Voltammetric Studies.

Cyclic voltammetry data of **2** and **3** are shown in Figure V-17 and V-18 respectively. In each case a prominent reduction peak is observed around -703 to -707 mV region corresponding to the metal-centred reduction Ni(II)(d<sup>8</sup>) → Ni(I)(d<sup>9</sup>); this process involves a small change in free energy as evident from the corresponding Frost diagram [Scheme IV-11]. This has been verified in chapter IV through isolation (NaBH<sub>4</sub> reduction) and characterization of the relevant Ni(I) complexes. A ligand-centred reduction peak is observed around -1376 mV to 1403 mV region. A

few reoxidation peaks can also be identified. In case of **2** such peaks appear at -550 mV and 822 mV respectively. For **3** such reoxidation peaks appears at -567 mV and 75 mV, respectively. A closer look at Figure V-18 indicates a near approach to quasi-reversible behavior for the metal-centred reduction-reoxidation couple ( $\Delta E_p = 138$  mV). The almost planar 'pn' chelate ring of **3** (Figure V-7) is possibly more effective in protecting the electrogenerated Ni(I) species from solvent attack. The extent of puckering of the 'pn' chelate ring (of **2** and **3**) in controlling the kinetic properties, is further illustrated by the kinetic data (UV-Vis spectroscopy), presented in the next section.

### Reactivity of **2** and **3** towards imidazole

Each of **2** and **3** possesses an aquo group and the group transfer reaction of the aquo group by imidazole (Im) will be interesting. As pointed out earlier imidazole is linked with histidine, which is a versatile coordinating agent towards the first transition metal in the biological systems. A typical reaction scheme e.g., for **2** (Scheme V-7) is shown below.



**Scheme V-7**

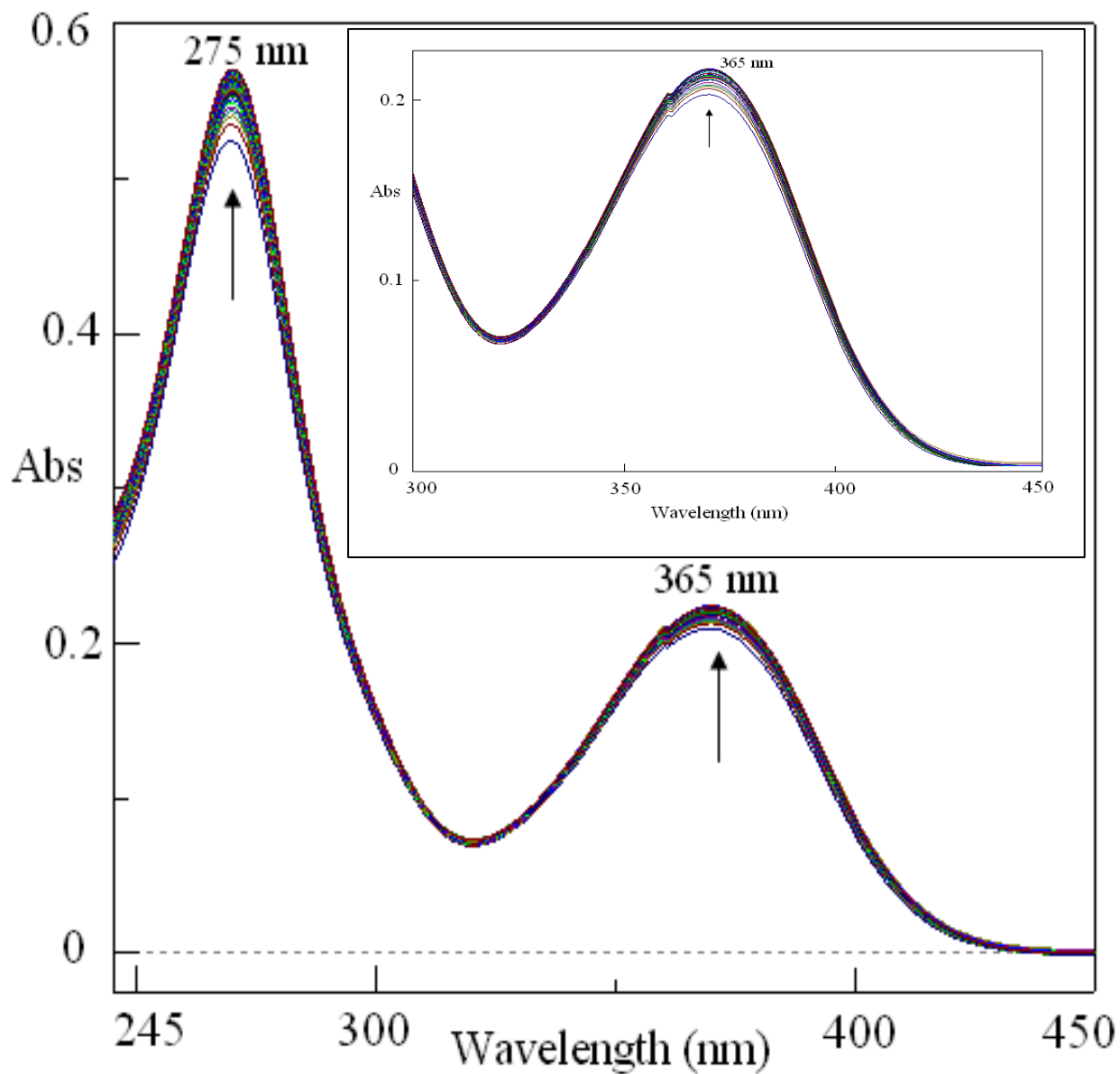


**Figure V-19.** Absorption spectral changes recorded at 2 min interval during the reaction of (2) ( $5.8 \times 10^{-5} \text{M}$ ) with Im ( $4.8 \times 10^{-3} \text{M}$ ) in  $\text{CH}_3\text{OH}$  at 311K

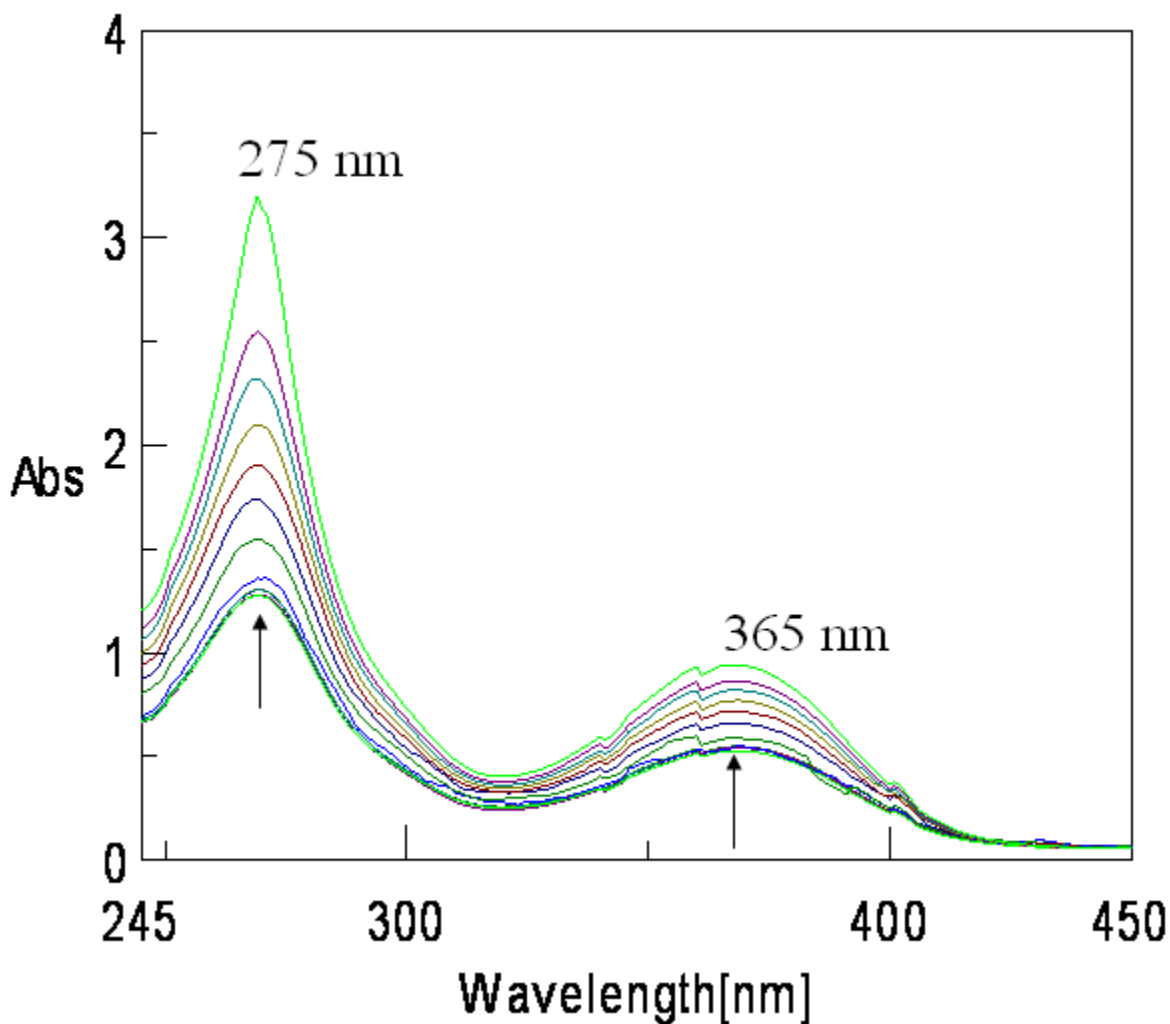


**Figure V-20.** Absorption spectral changes recorded at 4.5 min interval during the reaction of (3) ( $4.8 \times 10^{-5} \text{M}$ ) with Im ( $4.68 \times 10^{-3} \text{M}$ ) in  $\text{CH}_3\text{OH}$  at 313K

Stoichiometry of this reaction has been established in one case through the isolation and x-ray structural characterization of the corresponding imidazole substituted Ni(II) complex (Figure IV-1 and IV-2). The reaction profiles (overlay scans) are shown in Figure V-19 and V-20 respectively. Kinetics of these reactions were followed at 365 nm and four different temperatures in the range 308 – 328K under pseudo-first-order conditions (keeping ca. 100 times excess of the imidazole ligand). Observed rate constants were determined least square method

from the plots of  $\log(A_t - A_\infty)$  versus time, which were linear for 3 half-lives.<sup>49,50,92</sup> The relevant data are indicated below:

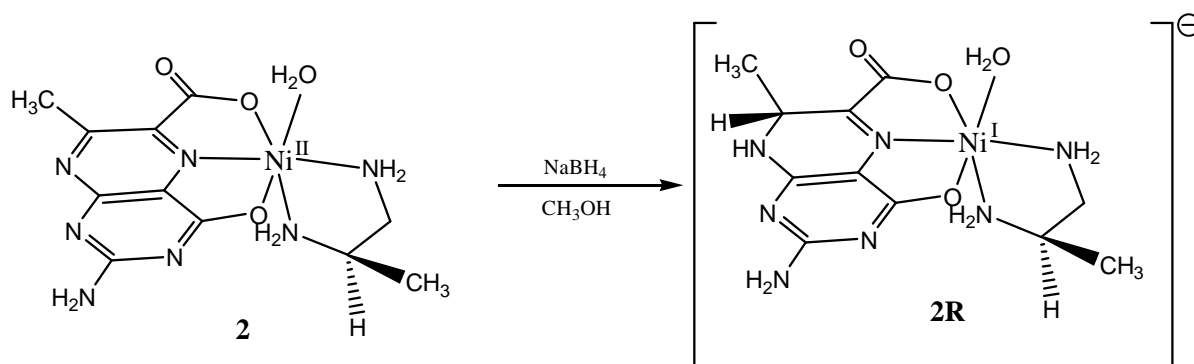
$$\text{For } \mathbf{2}: k_{\text{obs}} = 3.4 \times 10^{-3} \text{ s}^{-1}; \quad \Delta S^\ddagger = -198 \text{ J mol}^{-1} \text{ deg}^{-1};$$

$$\text{For } \mathbf{3}: k_{\text{obs}} = 3.9 \times 10^{-3} \text{ s}^{-1}; \quad \Delta S^\ddagger = -218 \text{ J mol}^{-1} \text{ deg}^{-1}.$$

The above data are commensurable with a ligand substitution process involving an associative pathway.<sup>97,98</sup> Such data together with Figure V-19 and V-20 illustrate the 'pn' chelate ring conformational control (Figure V-7) of the ligand substitution process here.

### Redox reactions of **2** and **3** with $\text{NaBH}_4$

It has been presented in chapter IV that treatment of a Ni(II) complex in  $\text{CH}_3\text{OH}$  medium with a slight excess of  $\text{NaBH}_4$  affords a dark-colored compound; physico-chemical studies pointed towards the formation of a Ni(I) complex with the 7, 8- dihydro form ( $\text{L}^{2-}$ ) of the pterin ligand residue, that is  $\text{NaBH}_4$  reduction affects only the pyrazine part of the pterin ring. In the present case, such reduced forms are termed as **2R** and **3R** respectively. The reaction profile (Scheme V-8) leading to the formation of **2R** and **3R** from **2** and **3** are shown in Figure V-21 and V-22, respectively.



**Scheme V-8**

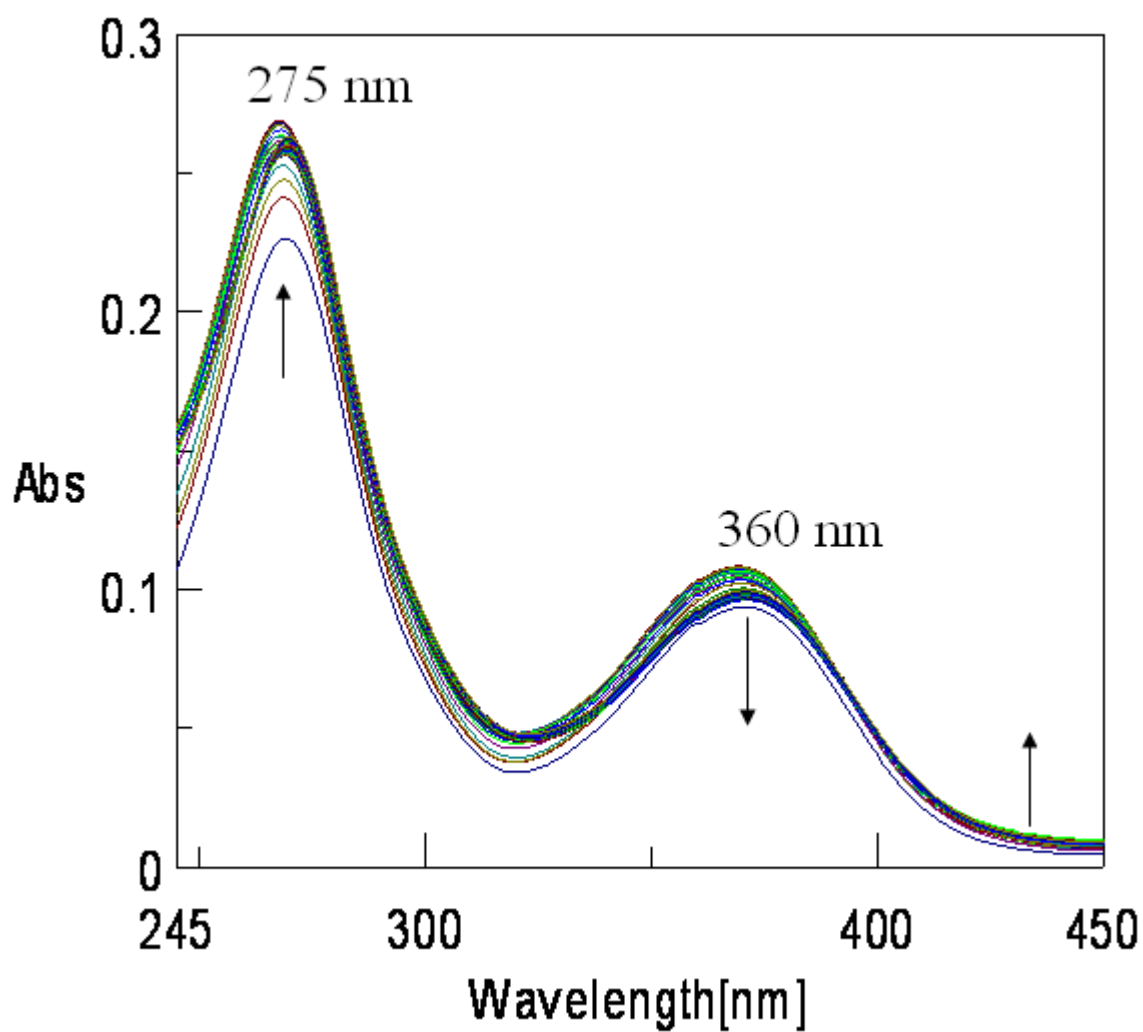


**Figure V-21.** Absorption spectral changes recorded at 1.5 min interval during the reaction of (2) ( $3.5 \times 10^{-5} \text{M}$ ) with  $\text{NaBH}_4$  ( $2.35 \times 10^{-3} \text{M}$ ) in  $\text{CH}_3\text{OH}$

---

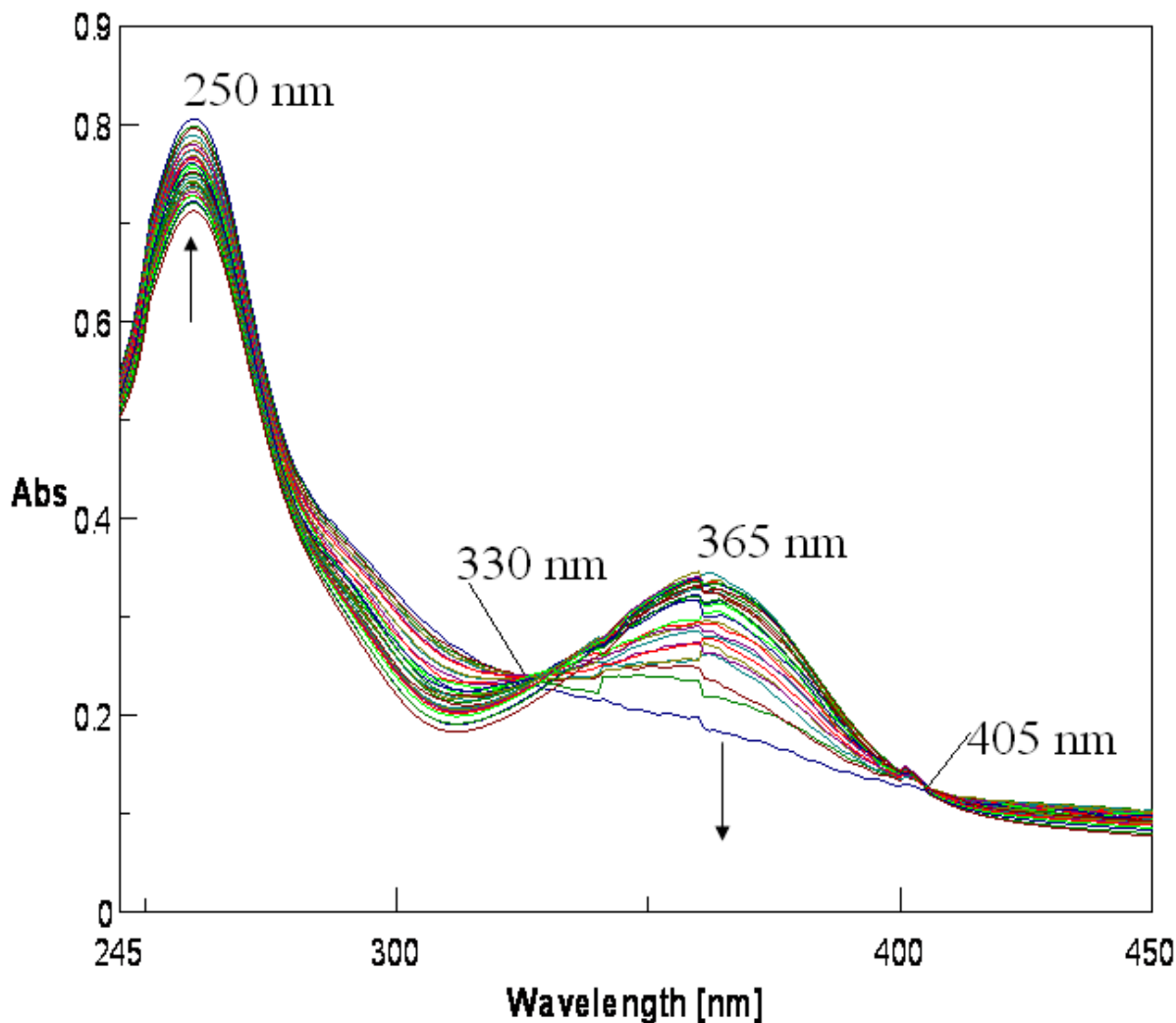


**Figure V-22.** Absorption spectral changes recorded at 1.5 min interval during the reaction of **3** ( $4.8 \times 10^{-5} \text{M}$ ) with  $\text{NaBH}_4$  ( $2.55 \times 10^{-3} \text{M}$ ) in  $\text{CH}_3\text{OH}$

They involve simultaneous reductions of the metal [ $\text{Ni(II)} \rightarrow \text{Ni(I)}$ ] and pterin [aromatic/oxidized state  $\rightarrow$  7, 8- dihydro state] ligand centres. The two  $\lambda_{\text{max}}$  values around 250 – 275 nm and 360 – 365 nm [ Figure V-21 and V-22] correspond to the  $\pi \rightarrow \pi^*$  (pterin) and LMCT (pterin  $\rightarrow$  metal) transitions. While Figure V-21 is devoid of any isosbestic point, Figure V-22 possesses such an attribute at 405 nm and close approach such a property around 330 nm; most likely the change over in oxidation state of the pterin ring is responsible for this observation, that

is, the spread out at 330 nm. For **3** the NaBH<sub>4</sub> reduction leading to the formation of **3R**, is essentially a one-step process. Kinetics of this reaction (Scheme V-8) were followed at 360 nm (365 nm for **3**) and four different temperatures in the range 300 – 330K in CH<sub>3</sub>OH under pseudo-first-order conditions ( with a **2/3** : NaBH<sub>4</sub> ratio of 1 : 140) and the pertinent kinetic parameters are stated below:

$$\text{For } \mathbf{2}: k_{\text{obs}} = 3.4 \times 10^{-3} \text{ s}^{-1}; \quad \Delta S^{\ddagger} = -208 \text{ Jmol}^{-1} \text{ deg}^{-1};$$

$$\text{For } \mathbf{3} \quad k_{\text{obs}} = 3.8 \times 10^{-3} \text{ s}^{-1}; \quad \Delta S^{\ddagger} = -228 \text{ Jmol}^{-1} \text{ deg}^{-1}.$$

The simultaneous group and electron transfer steps take place through associative pathway and once again highlight the ‘pn’ chelat ring conformational control of such reactions. The following redox reactions verify the reduced nature of **2R** and **3R**.

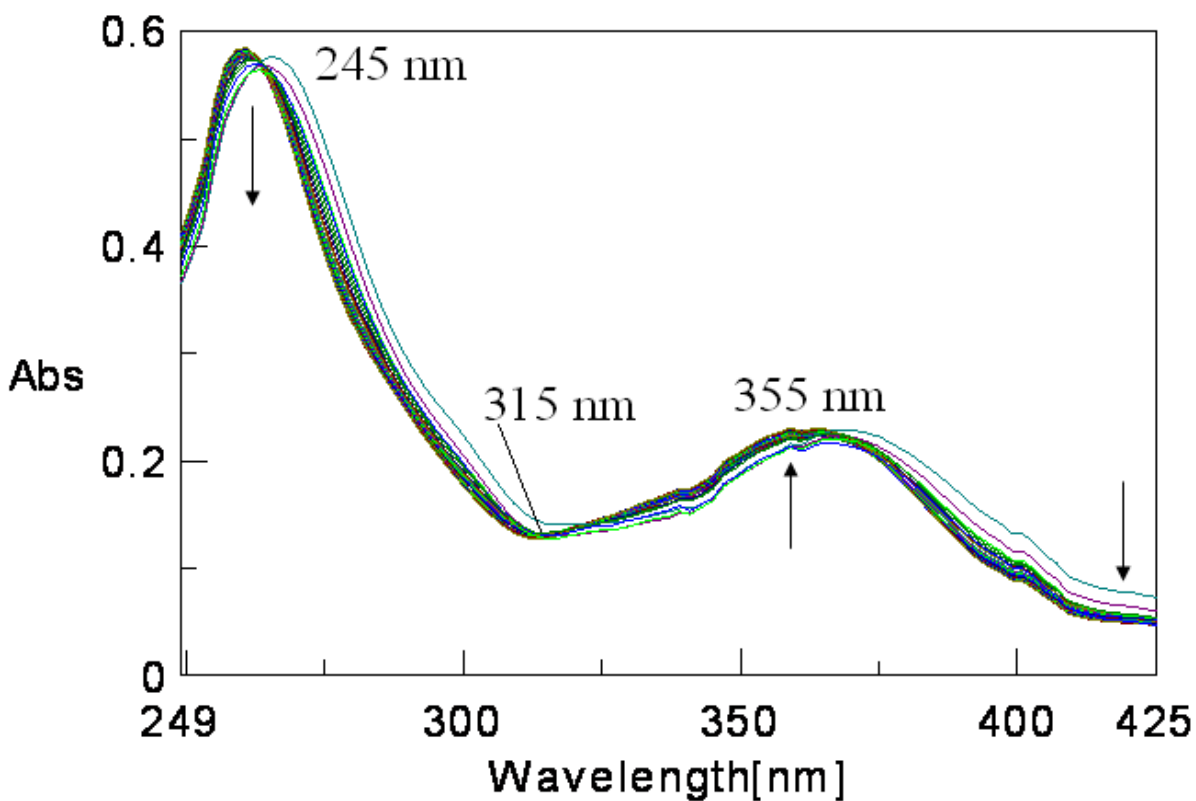


**Figure V-23.** Absorption spectral changes recorded at 15 second interval during the reaction of **2R** ( $3.5 \times 10^{-5} \text{M}$ ) with  $\text{K}_3\text{Fe}(\text{CN})_6$  ( $3.68 \times 10^{-3} \text{M}$ ) in  $\text{CH}_3\text{OH}$  at 298K

---

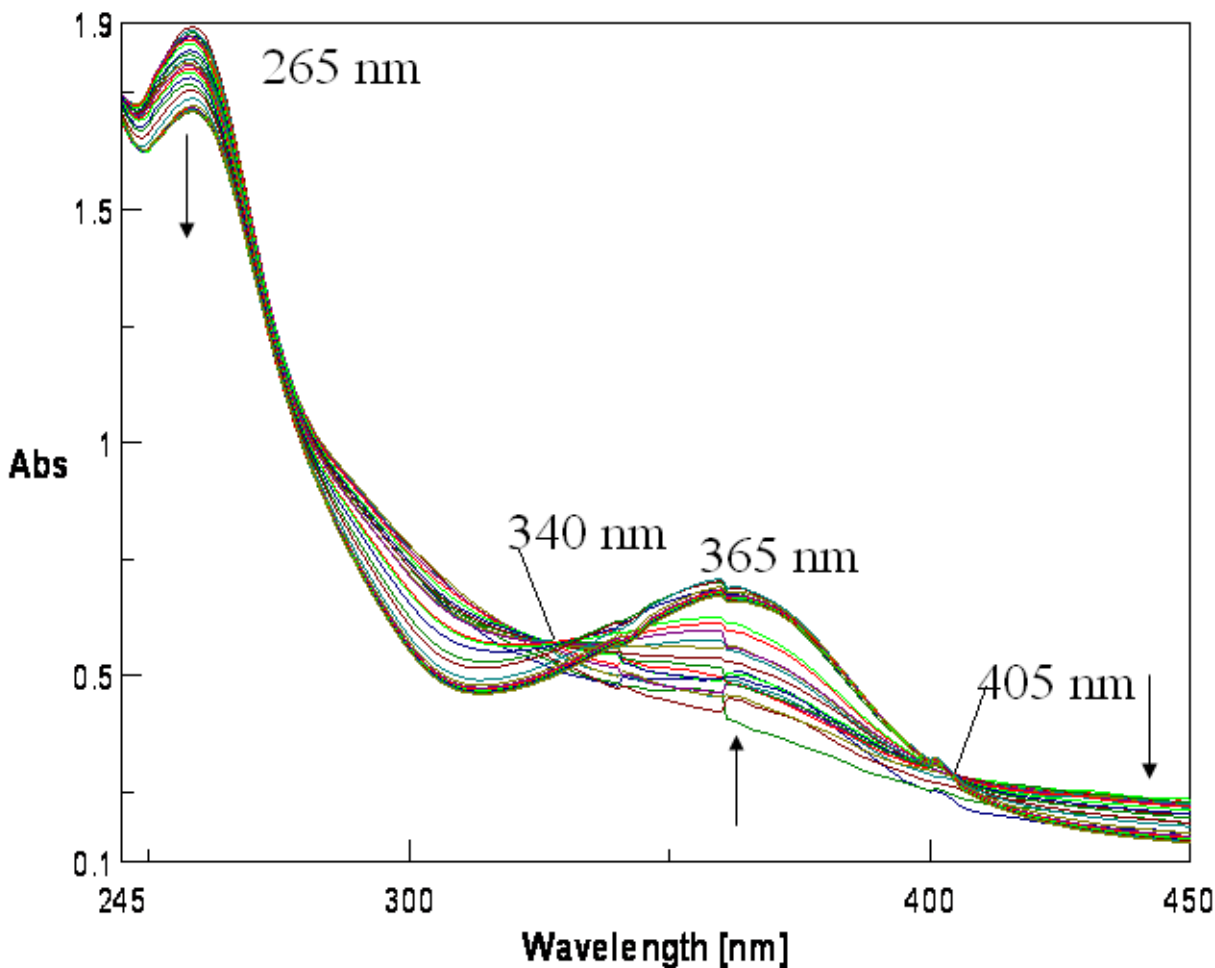


**Figure V-24.** Absorption spectral changes recorded at 15 second interval during the reaction of **3R** ( $4.8 \times 10^{-5} \text{M}$ ) with  $\text{K}_3\text{Fe}(\text{CN})_6$  ( $2.68 \times 10^{-3} \text{M}$ ) in  $\text{CH}_3\text{OH}$  at 298K

---

#### Reactions of **2R** and **3R** with $\text{K}_3[\text{Fe}(\text{CN})_6]$

The one-electron oxidant  $\text{K}_3[\text{Fe}(\text{CN})_6]$  is widely used for probing biochemical redox systems.<sup>94</sup> Its reaction profiles with **2R** and **3R** are shown in Figure V-23 and V-24

respectively; of them only Figure V-23 is characterized by an isosbestic point at 315 nm. Kinetics of this reaction was followed at 355 nm (365 nm for **3**) and four different temperatures (range 300 – 330K) in CH<sub>3</sub>OH under pseudo-first-order conditions (with a **2R/3R** : K<sub>3</sub>[Fe(CN)<sub>6</sub>] ratio of 1 : 140) and the relevant data are presented below:

$$\text{For } \mathbf{2R}: \quad k_{\text{obs}} = 1.7 \times 10^{-2} \text{ s}^{-1}; \quad \Delta S^{\ddagger} = -179 \text{ J mol}^{-1} \text{ deg}^{-1};$$

$$\text{For } \mathbf{3R} \quad k_{\text{obs}} = 2.2 \times 10^{-2} \text{ s}^{-1}; \quad \Delta S^{\ddagger} = -189 \text{ J mol}^{-1} \text{ deg}^{-1}.$$

The above  $k_{\text{obs}}$  data are faster by a power of ten than the previous results, most likely due to the pure electron transfer nature of K<sub>3</sub>[Fe(CN)<sub>6</sub>]. The initial oxidized species may undergo further reactions as evident from the reaction profile of **3R** (Figure V-24), lacking any isosbestic point.

Again, the absorption spectral studies indicate (Figure IV-26) that NaBH<sub>4</sub> is unable to react with K<sub>3</sub>[Fe(CN)<sub>6</sub>], but both **2R** and **3R** do as the present data indicate. In other words, **2** and **3** are able to mediate the transfer of reducing equivalents from NaBH<sub>4</sub> to K<sub>3</sub>[Fe(CN)<sub>6</sub>] through **2R** and **3R**. An analogy may be drawn (of **2/2R** as well as **3/3R**) with the NAD<sup>+</sup>/NADH couple, which is a typical biochemical mediator.<sup>94</sup> NAD<sup>+</sup> can be reduced nonenzymatically by NaBH<sub>4</sub>, whereas NADH can in turn be nonenzymatically reoxidized with K<sub>3</sub>[Fe(CN)<sub>6</sub>], but not by molecular O<sub>2</sub>. A major factor responsible for such unique redox property of **2** and **3** (as well as of **2R** and **3R**) is the presence of the redox non-innocent pterin ring (its pyrazine part) which can exist in a couple of oxidation states. This aspect is accentuated by the redox active metal centre and further such redox property of the same metal-pterin entity can be fine tuned by the chiral ancillary ligand as evident from Figure V-21 to V-24. This has direct bearing on the pterin-containing metalloenzymes where such fine tuning of property of the metal-pterin unit is possible by the donor atom of the protein backbone.<sup>103</sup>

### **Reactivity of 2R and with bromobenzene and dioxygen.**

For exploring the ability of **2R** to model phenylalanine hydroxylase type (PAH) activity, its reactivity towards a reaction mixture of bromobenzene and dioxygen has been studied. Here bromobenzene is used as a model substrate (instead of phenylalanine) for its ease of handling, facilitating the recovery of the corresponding product (i.e., 4-bromophenol) and its characterization. Figure V-25 shows the relevant reaction profile; here the arrows showing the movements of

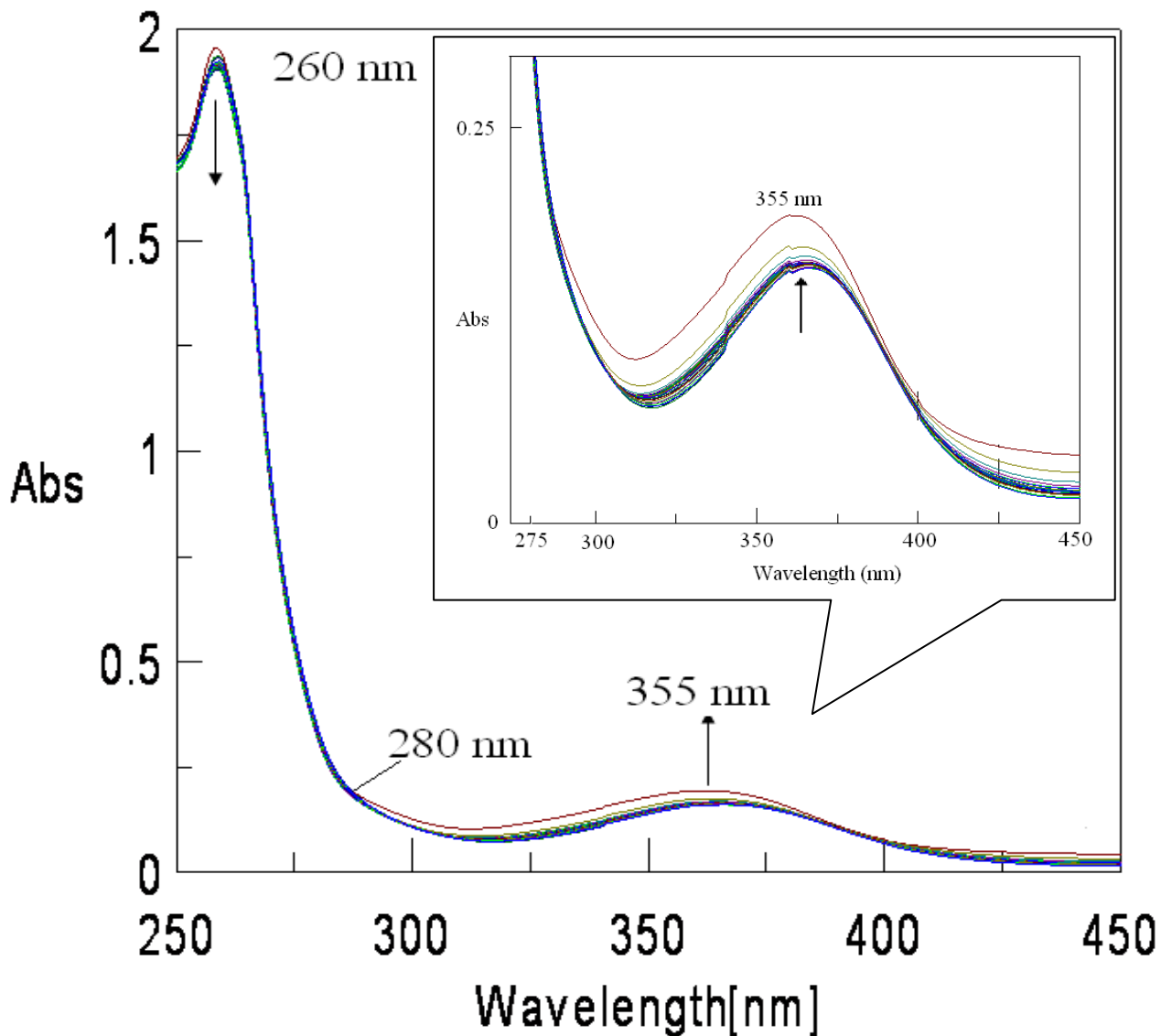
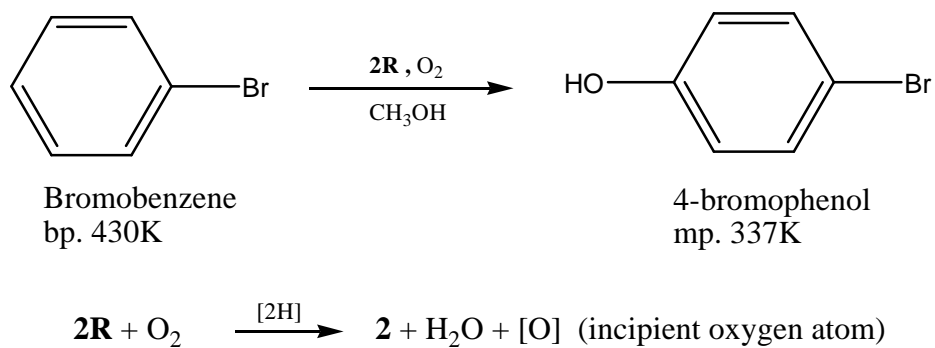


**Figure V-25.** Absorption spectral changes recorded at 2 min interval at 303K during the reaction of **(2R)** ( $3.5 \times 10^{-5} \text{M}$ ) with bromobenzene ( $3.54 \times 10^{-3} \text{M}$ ) in  $\text{CH}_3\text{OH}$  saturated with  $\text{O}_2$ .

the absorption spectral curves represent an opposite behavior to those in Figure V-21, (reflecting the  $\text{NaBH}_4$  reduction of **2** to **2R**). Scheme V-9 summarizes the above-mentioned redox reaction leading to the hydroxylation of the aromatic ring of bromobenzene (a model of PAH reaction);



**Scheme V-9**

the role of **2R** (or specifically its 7, 8-dihydro form of the pterin ligand residue, L<sup>2-</sup>) in supplying two reducing equivalents, [2H] to O<sub>2</sub> is apparent. Kinetics of this reaction (Figure V-25) was followed at 355 nm and four different temperatures (range 300 – 330 K) in CH<sub>3</sub>OH saturated with O<sub>2</sub> under pseudo-first-order conditions (with a **2R** : bromobenzene ratio 1 :140) and the kinetic parameters are shown below:

For **2R**:  $k_{\text{obs}} = 2.6 \times 10^{-3} \text{ s}^{-1}$ ;  $\Delta S^\ddagger = - 228 \text{ Jmol}^{-1} \text{ deg}^{-1}$ ;

For **3R**  $k_{\text{obs}} = 2.1 \times 10^{-3} \text{ s}^{-1}$ ;  $\Delta S^\ddagger = - 238 \text{ Jmol}^{-1} \text{ deg}^{-1}$ .

The above kinetic parameters are summarized in Table V-6.

**Table V-6.** Comparison of kinetic parameters for the reactions of **2**, **2R** & **3**, **3R** with different substrates

Compound	Kinetic parameters	Reaction with Imidazole (2/3)	Reaction with bromobenzene (2R/3R)	Reaction with K <sub>3</sub> [Fe(CN) <sub>6</sub> ] in CH <sub>3</sub> OH-H <sub>2</sub> O 3:1 v/v (2R/3R)	Reaction with NaBH <sub>4</sub> in CH <sub>3</sub> OH (2/3)
<b>2</b>	k <sub>obs</sub> <sup>(a)</sup> (s <sup>-1</sup> )	3.4x10 <sup>-3</sup>	2.6 x10 <sup>-3</sup>	1.7x10 <sup>-2</sup>	3.4 x10 <sup>-3</sup>
	ΔS <sup>‡</sup> (JK <sup>-1</sup> mol <sup>-1</sup> )	-198	-228	-178	-208
<b>3</b>	k <sub>obs</sub> <sup>(a)</sup> (s <sup>-1</sup> )	3.9x10 <sup>-3</sup>	2.1 x 10 <sup>-3</sup>	2.2 x10 <sup>-2</sup>	3.8 x10 <sup>-3</sup>
	ΔS <sup>‡</sup> (JK <sup>-1</sup> mol <sup>-1</sup> )	-218	-238	-189	-228

### Electronic structures of 2 and 3 : Correlation with reactivity

The electronic structures of **2** and **3** have been obtained by DFT calculations, using their x-ray structural data as input parameters for the Gaussian 09 program. The energies (eV) and composition(%) of few frontier MOs are shown in Figure V-26. A small band gap (ΔE = 0.19 eV) is observed between the HOMO and HOMO-1 levels of **2**; again an energy difference of 0.56 eV exists between the LUMO and LUMO +1 levels. On the other hand for **3** LUMO and LUMO+1 levels have an energy gap of 0.19eV. As stated earlier synthetic molecules with

exceptionally small (0.5 eV) HOMO – LUMO gaps are receiving attention due to their interesting electrochemical / redox amphoteric behavior.<sup>64,66</sup> Usually in such cases the HOMO – LUMO orbitals are located in different covalently linked centers in a single molecule. Thermoexcited intramolecular electron transfer may occur between two such centers in solution. Most likely the combination of the redox non-innocent pterin ligand residue with the redox active metal centre [Ni(II)/Ni(I)] in complexes **2** and **3**, lead to such a situation here associated with distinct redox activities.<sup>9-11,53</sup> For example, reducing equivalents can be transferred with ease into the LUMO, LUMO + 1 levels of **2** and **3**, during reaction with NaBH<sub>4</sub>. On the other hand, the HOMO and HOMO-1 levels of **2** are associated with a small band gap, a property not shared by **3**. As a result the release of reducing equivalents from **2R** and **3R** [during reactions with K<sub>3</sub>[Fe(CN)<sub>6</sub>] and bromobenzene/O<sub>2</sub>] should be different kinetically. Figure V-23 to V-25 illustrate this aspect.

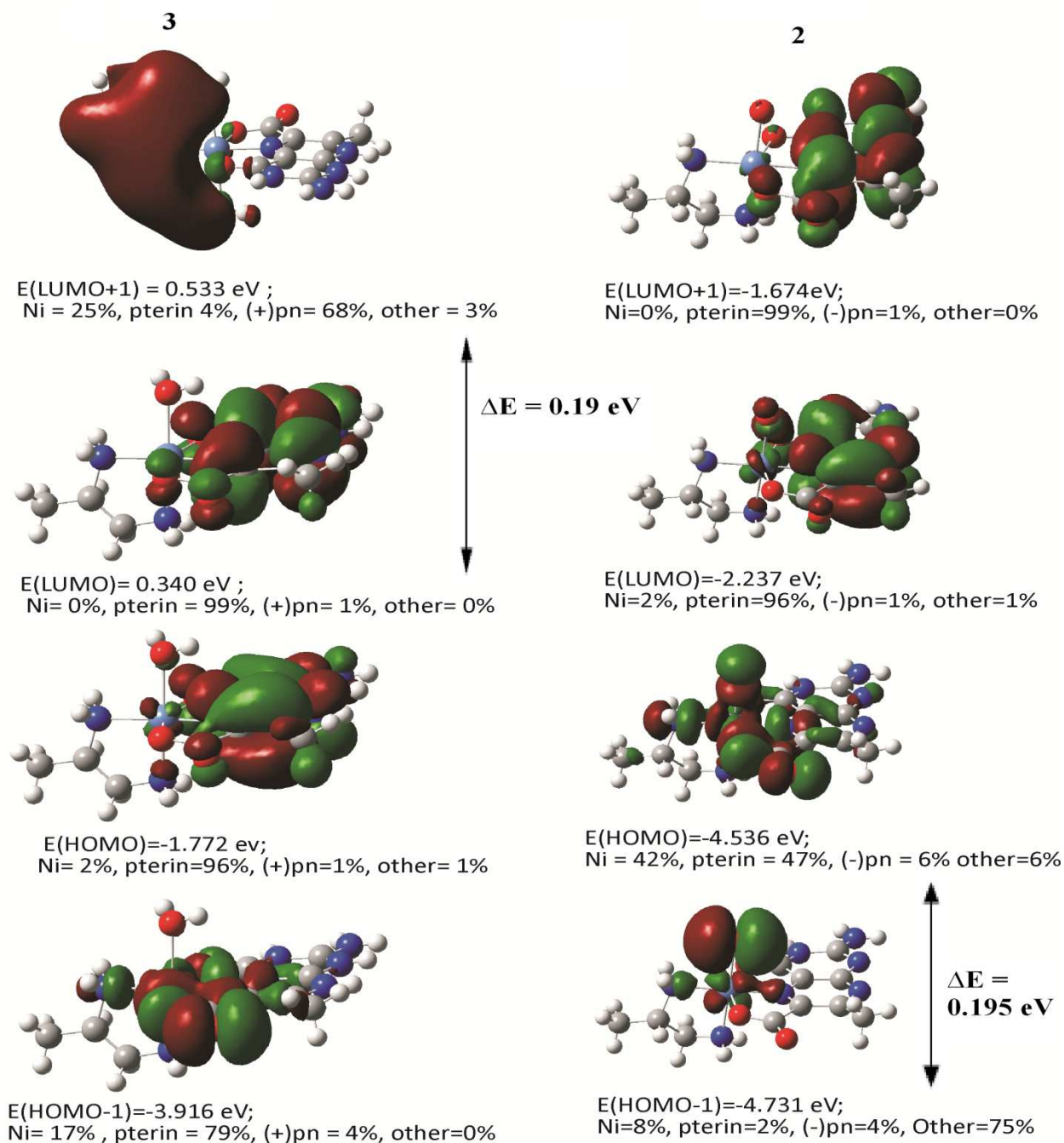


**Figure V-26.** Frontier molecular orbitals of **2** and **3**, showing their energies (eV) and compositions (%).

## Conclusion

This chapter is centered on two chiral mixed ligand Ni(II)-pterin complexes. They possess identical chemical composition and the ancillary ligands (pn) confers chirality on them through conformational contribution ( $\delta/+$ ). Their cyclic voltammetric data as well as reactivities towards imidazole, NaBH<sub>4</sub> and also of their reduced forms (**2R** & **3R**) towards K<sub>3</sub>[Fe(CN)<sub>6</sub>] and bromobenzene/O<sub>2</sub>, highlight the conformational control of metal and pterin based group and / electron transfer reactions. The above aspect is significant in understanding the reactions catalysed by pterin-containing metalloenzymes, where donor atoms from the protein back bone play a significant role in controlling the redox properties of the metal centre.